

2023

Synthesis And Characterization Of Two Sets Of Group 12 Complexes With Organic Ligands

Michelle Sturner

William & Mary - Arts & Sciences, masturner03@gmail.com

Follow this and additional works at: <https://scholarworks.wm.edu/etd>

 Part of the [Chemistry Commons](#)

Recommended Citation

Sturner, Michelle, "Synthesis And Characterization Of Two Sets Of Group 12 Complexes With Organic Ligands" (2023). *Dissertations, Theses, and Masters Projects*. William & Mary. Paper 1697552671.
<https://dx.doi.org/10.21220/s2-ytgp-2895>

This Thesis is brought to you for free and open access by the Theses, Dissertations, & Master Projects at W&M ScholarWorks. It has been accepted for inclusion in Dissertations, Theses, and Masters Projects by an authorized administrator of W&M ScholarWorks. For more information, please contact scholarworks@wm.edu.

Synthesis and Characterization of Two Sets of Group 12 Complexes With
Organic Ligands

Michelle Sturner

Alexandria, VA

B.S Chemistry, William & Mary, 2018

A Thesis presented to the Graduate Faculty of The College of William &
Mary in Candidacy for the Degree of
Master of Science

Department of Chemistry

College of William & Mary
August, 2023

APPROVAL PAGE

This Thesis is submitted in partial fulfillment of
the requirements for the degree of

Master of Science

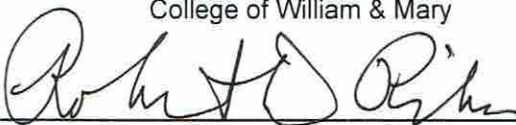


Michelle Sturner

Approved by the Committee, April 2023



Committee Chair or Co-Chair
Deborah Bebout, Professor, Chemistry
College of William & Mary



Robert Pike, Professor, Chemistry
College of William & Mary



William McNamara, Associate Professor, Chemistry
College of William & Mary

ABSTRACT

The complexes of group 12 elements are subjects of incredible interest due to differences in their bioactivity. Zinc is an essential element of life and is required for many bodily processes including gene production, growth, and the immune response. Cadmium and mercury are both toxic elements to humans. Part of their activity is due to their ability to replace zinc metal centers. Synthesis of new group 12 complexes can provide insight regarding their bioactivity and how replacement of metal centers can affect the structure of enzymes. In this thesis, the preparation and characterization of two sets of group 12 complexes is described.

One set of new complexes are cadmium and mercury complexes of the N₃S ligand 2-[bis(2-pyridinylmethyl)amino]ethanethiol (**L1H**) with chemical formulas [Cd(**L1**)Cl]₂·benzene (**1**) and [Hg(**L1**)Cl] (**2**). They are compared with the known complex [Zn(**L1**)Cl] (**3**). The new complexes were thoroughly characterized using X-ray crystallography, XPRD, ¹H NMR, elemental analysis, and IR. Compound **1** crystallized in the triclinic space group *P*-1 with an octahedral coordination geometry. The metal ions of **1** were bridged by a pair of ligand thiolate groups. Mononuclear compound **2** crystallized in the monoclinic space group *P*2₁/*c* with mixed square pyramidal/trigonal bipyramidal geometry ($\tau = 0.44$). Both complexes are stabilized by significant offset face-to-face π - π and edge-to-face σ - π interactions between the pyridyl rings, and for **1**, between the pyridyl rings and solvent benzene in the unit cells. Significantly, both complexes exhibit heteronuclear coupling in the ¹H NMR at -40 °C between the metal centers and specific ligand protons indicating slow ligand exchange on the coupling constant time scale and unusual stability for thiolate complexes of these metal ions.

The other set of isolated complexes are bis-tridentate chelates of Zn(ClO₄)₂, Cd(ClO₄)₂, and Hg(ClO₄)₂ with two equivalents of bis(2-pyridylmethyl) ether (**L2**). The complexes were characterized using X-ray crystallography, IR, ¹H NMR, and TGA. [Zn(**L2**)₂](ClO₄)₂·CH₃CN (**4**) and [Cd(**L2**)₂](ClO₄)₂·CH₃CN (**5**) crystallized in the monoclinic space group *P*2₁ with meridional octahedral geometry. [Hg(**L2**)₂](ClO₄)₂ (**6**) crystallized with approximately C₂ symmetric trigonal prismatic geometry. ¹H NMR of **3** at -40 °C show heteronuclear *J*_{HgH} coupling, and lacks the geminal splitting of methylene protons that would be expected for the solid-state structure. The complexes were compared to other bis-tridentate chelates of bis(2-pyridylmethyl) ligands with the central oxygen of **L2** replaced by other heteroatoms.

TABLE OF CONTENTS

Acknowledgements	ii
Introduction	1
References	7
Structural Comparison of Group 12 Complexes of a Tripodal Mixed NS(thiolato) Donor Ligand	
Introduction	10
Experimental	14
Results and Discussion	19
Conclusion	35
References	36
Synthesis and characterization of bis-tridentate group 12 perchlorate complexes of bis(2-pyridylmethyl) ether	
Introduction	39
Experimental	42
Results and Discussion	48
Conclusion	65
References	66

ACKNOWLEDGEMENTS

I would like to thank Dr. Deborah Bebout, whose guidance, insight, and patience helped me throughout the process of researching and writing this thesis. I would also like to thank Dr. Robert Pike, whose expertise with X-ray diffraction was helpful to my research. I also thank Dr. William McNamara for being patient with me despite me making his job of Director of Graduate Studies much harder.

I also thank Ian Starr and Joshua Owusu for contributing to the work presented, and countless past members of the Bebout lab whose work provided a foundation for this thesis.

Thank you also to Mom, Dad, and Cate, whose support and love got me through this.

Chapter 1. Introduction

The elements of group 12 are of scientific interest due to their diverse biological roles. Zinc is an essential element to all forms of life and is the second most abundant transition metal in living organisms after iron [1]. Divalent zinc plays important roles in gene expression, reproduction, growth, and immunity as a common metal center in many proteins [2,3]. Excess zinc can be toxic, however. Effects of zinc toxicity include nausea, diarrhea, and neuron death. Excess zinc can also cause copper deficiency. Expression of metallothionein is increased to help regulate zinc levels, but also prevent the absorption of copper [4]. Meanwhile cadmium and mercury are both very toxic.

Cadmium pollution is a significant concern. Cadmium is ranked seventh on the 2022 Substance Priority List by the Agency for Toxic Substances and Disease Registry (ATSDR), signaling both its toxicity and prevalence [5]. The World Health Organization lists cadmium as being one of ten chemicals with major public health concerns [6]. Anthropogenic sources of cadmium include iron and steel smelting, fossil fuel burning, tobacco smoke, and phosphate fertilizers [7]. Foods such as vegetables, grains (particularly rice), and shellfish accumulate cadmium quickly and are large dietary sources [8,9]. Cadmium exposure can cause various cancers, osteoporosis, and various liver and kidney diseases [10]. An infamous outbreak of cadmium poisoning, known as Itai-Itai disease, occurred in the early-mid 1900s around the Jinzu River basin in Toyama Prefecture, Japan. Zinc mine

waste containing cadmium was discharged into the river, causing osteomalacia, osteoporosis, and kidney failure in residents [11].

Mercury pollution is of similar or greater concern to cadmium pollution. The ATSDR puts it third on its 2022 Substance Priority List, for both its greater toxicity and greater prevalence as a pollutant [5]. The WHO also lists mercury as one of their ten chemicals of major public health concern [6]. Mercury is present as a pollutant in its elemental form (Hg^0), its inorganic form (Hg_2^{2+} and Hg^{2+}), and as methylmercury. Natural sources of elemental mercury pollution include volcanic eruptions and forest fires. Anthropogenic sources of elemental mercury include fossil fuel burning, mine waste, and cement production [12]. Elemental mercury can easily bypass the blood brain barrier and the lipid bilayers of cells and cell organelles [13]. Once inside the cell, Hg^0 can be oxidized to Hg^{2+} which quickly reacts with enzymes, GSH, and other intracellular molecules, inhibiting their function and causing oxidative stress. Methylmercury is formed from the biomethylation of inorganic mercury by aquatic bacteria. The toxicity of methylmercury is caused by its high affinity with thiol and seleno groups [13]. Methylmercury binding with those nucleophilic groups can hinder the function of proteins. The binding of seleno groups can hinder the ability of selenoenzymes to properly protect against oxidative damage to the nervous system [13]. This can lead to various neurodegenerative diseases such as Alzheimer's and ALS [13].

Zinc-containing proteins are common, and the majority of zinc proteins are enzymes. A 2012 bioinformatic study by Andreini and Bertini found that about 80% of zinc-containing proteins in bacteria and archaea and slightly over 50% in

eukaryotes were enzymes¹ [14]. This difference can be ascribed to how common zinc fingers are in eukaryotic protein structures. That same 2012 study found that over 50% of all zinc-containing enzymes were hydrolases. The remaining were roughly split between the other enzyme classes [14]. Hydrolases make an even larger percentage of total zinc-containing enzymes in bacteria and archaea due to zinc-containing β -lactamase, which are absent in eukaryotes. In 2012, about three-quarters of the enzymatic zinc metal centers had a catalytic function while the others were solely structural [14]. In the resting state, the coordination geometries of structurally characterized enzymatic zinc centers were split between tetrahedral and trigonal bipyramidal geometry. In contrast, zinc metal centers associated with a catalytic reaction in progress were mainly five coordinate, with most being trigonal bipyramidal [14].

The most common amino acids coordinated to zinc metal centers are histidine, cysteine, aspartate, and glutamate. In each enzyme class, histidine is one of the most common amino acids. It was the most common amino acid bound to zinc in lyases, oxidoreductases, and hydrolases and had roughly equal distribution with one or more other amino acids in other enzyme classes in 2012 [14]. In contrast, cysteine occurred in around 30–45% of ligases, oxidoreductases, and transferases, but was found rarely in hydrolases and not all in isomerases as of the 2012 review. The relative occurrence of amino acids also depended on whether the zinc metal center had a structural or catalytic role. The 2012 study by

¹ While the number of characterized proteins has increased since 2012, this study can still give a rough idea about statistics regarding zinc-containing proteins.

Andreini and Bertini found that while cysteine occurred in only slightly over 10% of catalytic sites, it occurs in almost three-quarters of structural sites [14].

Due to the complexity of proteins, small molecule models can be useful for gaining insight regarding the structure or catalytic mechanism of metal centers [15]. For example, the enzyme metallo- β -lactamase in *B. fragilis* has been found to have a water-bridged dinuclear zinc active site. One zinc atom has tetrahedral coordination from three histidines and a water molecule. The second zinc is trigonal bipyramidal and coordinated by a histidine, aspartate, a cysteine, and two water molecules, one of them being the bridging water [16]. Kurosaki *et al.* prepared a zinc chloride complex of the tripodal N₃S ligand 2-[bis(2-pyridinylmethyl)amino]ethanethiol (**L1H**), shown in Figure 1, to investigate the purpose of the thiol in the catalytic activity of the metal center [17]. The resulting complex [Zn(**L1**)Cl] was found to undergo an equilibrium between a monomer and dimer form. A gradual decrease in hydrolysis activity, like that catalyzed by metallo- β -lactamase, at higher concentration suggests that the monomer form is the active species. The thiol served to stabilize the dimer form and contributes to lower overall hydrolytic activity [17].

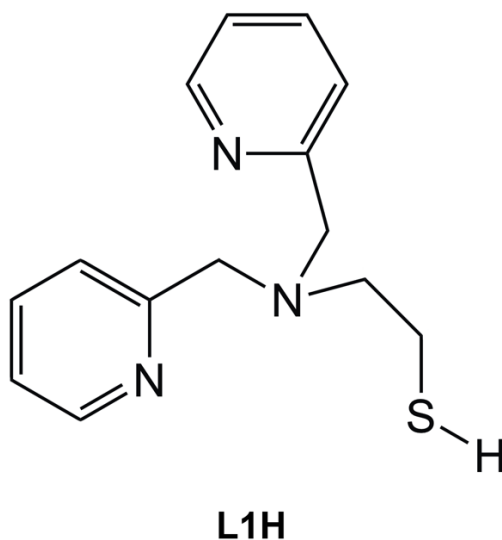


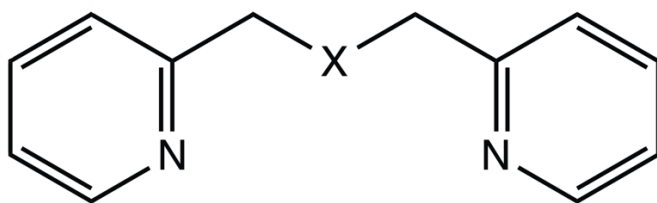
Figure 1. Structure of **L1H**.

The studies described in this thesis were inspired by the ways mercury and cadmium can negatively effects proteins and how small molecular models can potentially provide insight regarding the effect of xenobiotic metal ions on proteins. Both mercury and cadmium are associated with protein misfolding and aggregation [18]. Mercury and cadmium can also replace zinc centers in proteins, sometimes with greater affinity than zinc, and can greatly reduce enzyme activity [19-21]. Comparing complexes of group 12 metal ions with the same ligand can provide insight into how replacement of zinc with cadmium or mercury can affect the structure of metal centers.

The chapters in this thesis present two sets of group 12 complexes, each a possible model for different types of protein metal centers. In Chapter 2, cadmium and mercury complexes with the N₃S ligand **L1H** are characterized and compared to each other and to the zinc complex synthesized by Kurosaki *et al.* [17]. As

mentioned earlier, $[\text{Zn}(\text{L1})\text{Cl}]$ has already been used as a potential model for metallo- β -lactamase. The prevalence of histidine- and cysteine-containing zinc metal centers suggest that zinc complexes of **L1H** could potentially serve as model complexes of other metalloproteins.

In Chapter 3, complexes of zinc, cadmium, and mercury perchlorate salts with the ether-containing ligand bis(2-pyridylmethyl) ether (**L2**), shown in Figure 2, are characterized. Ether-containing bioactive compounds with metal dependent bioactivity, such as flavonoids [22,23], ionophores [24-26], and carbohydrates are common. Some of their functions include regulation of the bioaccumulation of group 12 metals [27,28]. Chapter 3 also compares the group 12 perchlorate complexes of **L2** with complexes of related bipyridyl ligands previously synthesized in the Bebout lab, **L3–L5** in Figure 2. Variations in the solid state structures of bis-tridentate chelates with central oxygen, nitrogen, sulfur, and selenium atoms are summarized.



L2	X = O
L3	X = N
L4	X = S
L5	X = Se

Figure 2. Structurally related N,X,N ligands.

References

- [1] MP Cuajungco, MS Ramirez, ME Tolmasky. Zinc: multidimensional effects on living organisms, *Biomedicines* 9 (2021) 208–232.
- [2] T Hara, T Takeda, T Takagishi, K Fukue, T Kambe, T Fukada. Physiological roles of zinc transporters: molecular and genetic importance in zinc homeostasis, *J. Physiol. Sci.* 67 (2017) 283–301.
- [3] CT Chasapis, PA Ntouna, CA Spiliopoulou, ME Stefanidou. Recent aspects of the effects of zinc on human health, *Arch. Toxicol.* 94 (2020) 1443–1460.
- [4] LM Plum, L Rink, H Haase. The Essential Toxin: Impact of Zinc on Human Health, *Int. J. Environ. Res. Public Health* 7 (2010) 1342–1365.
- [5] Agency for Toxic Substances and Disease Registry, ATSDR's Substance Priority List, (2022).
- [6] World Health Organization, 10 Chemicals of Public Health Concern, (2020).
- [7] BJ Alloway, E Steinnes, Anthropogenic additions of cadmium to soils, *Cadmium in soils and plants*, Springer, 1999, pp. 97–123.
- [8] S Satarug, JR Baker, S Urbenjapol, M Haswell-Elkins, PE Reilly, DJ Williams, MR Moore. A global perspective on cadmium pollution and toxicity in non-occupationally exposed population, *Toxicol. Lett.* 137 (2003) 65–83.
- [9] I Suhani, S Sahab, V Srivastava, RP Singh. Impact of cadmium pollution on food safety and human health, *Curr. Opin. Toxicol.* 27 (2021) 1–7.
- [10] G Genchi, MS Sinicropi, G Lauria, A Carocci, A Catalano. The effects of cadmium toxicity, *Int. J. Environ. Res. Public Health* 17 (2020) 3782–3805.
- [11] K Aoshima. Itai-itai disease: Renal tubular osteomalacia induced by environmental exposure to cadmium—historical review and perspectives, *Soil Sci. Plant Nutr.* 62 (2016) 319–326.
- [12] LT Budnik, L Casteleyn. Mercury pollution in modern times and its socio-medical consequences, *Sci. Total Environ.* 654 (2019) 720–734.
- [13] A Carocci, N Rovito, MS Sinicropi, G Genchi, Mercury Toxicity and Neurodegenerative Effects, in: Whitacre DM (Ed.), *Reviews of Environmental Contamination and Toxicology*, Springer International Publishing, Cham, 2014, pp. 1–18.

- [14] C Andreini, I Bertini. A bioinformatics view of zinc enzymes, *J. Inorg. Biochem.* 111 (2012) 150–156.
- [15] G Henkel, B Krebs. Metallothioneins: Zinc, Cadmium, Mercury, and Copper Thiulates and Selenolates Mimicking Protein Active Site Features – Structural Aspects and Biological Implications, *Chem. Rev.* 104 (2004) 801–824.
- [16] NO Concha, BA Rasmussen, K Bush, O Herzberg. Crystal structure of the wide-spectrum binuclear zinc β -lactamase from *Bacteroides fragilis*, *Structure* 4 (1996) 823–836.
- [17] H Kurosaki, T Tawada, S Kawasoe, Y Ohashi, M Goto. A model for ZnII-containing- β -lactamase: synthesis, X-ray crystal structure of a zinc(II) complex bearing thiol group and hydrolysis of phosphate diester, *Bioorg. Med. Chem. Lett.* 10 (2000) 1333–1337.
- [18] MJ Tamás, SK Sharma, S Ibbstedt, T Jacobson, P Christen. Heavy Metals and Metalloids As a Cause for Protein Misfolding and Aggregation, *Biomolecules* 4 (2014) 252–267.
- [19] AE Funk, FA Day, FO Brady. Displacement of zinc and copper from copper-induced metallothionein by cadmium and by mercury: In vivo and ex vivo studies, *Comp. Biochem. Physiol. Part - C: Toxicol. Pharmacol.* 86 (1987) 1–6.
- [20] L Tang, R Qiu, Y Tang, S Wang. Cadmium–zinc exchange and their binary relationship in the structure of Zn-related proteins: a mini review, *Metallomics*. 6 (2014) 1313–1323.
- [21] A Jancsó, B Gyurcsik, E Mesterházy, R Berkecz. Competition of zinc(II) with cadmium(II) or mercury(II) in binding to a 12-mer peptide, *J. Inorg. Biochem.* 126 (2013) 96–103.
- [22] K Sreenivasulu, P Raghu, KM Nair. Polyphenol-Rich Beverages Enhance Zinc Uptake and Metallothionein Expression in Caco-2 Cells, *J. Food Sci.* 75; 20090990 (2010) H123–H128.
- [23] E Kim, T Pai, O Han. Effect of Bioactive Dietary Polyphenols on Zinc Transport across the Intestinal Caco-2 Cell Monolayers, *J. Agric. Food Chem.* 59 (2011) 3606–3612.
- [24] J Ivanova, IN Pantcheva, M Mitewa, S Simova, M Tanabe, K Osakada. Cd(II) and Pb(II) complexes of the polyether ionophorous antibiotic salinomycin, *Chem. Cent. J.* 5 (2011) 52–59.

- [25] M Antoszczak, D Steverding, A Huczynski. Anti-parasitic activity of polyether ionophores, *Eur. J. Med. Chem.* 166 (2019) 32–47.
- [26] A Huczynski. Polyether ionophores-promising bioactive molecules for cancer therapy, *Bioorg. Med. Chem. Lett.* 22 (2012) 7002–7010.
- [27] X Li, X Jiang, J Sun, C Zhu, X Li, L Tian, L Liu, W Bai. Cytoprotective effects of dietary flavonoids against cadmium-induced toxicity, *Ann. N. Y. Acad. Sci.* 1398 (2017) 5–19.
- [28] W Zhang, J Zhi, Y Cui, F Zhang, A Habyarimana, C Cambier, P Gustin. Potentiated interaction between ineffective doses of budesonide and formoterol to control the inhaled cadmium-induced up-regulation of metalloproteinases and acute pulmonary inflammation in rats, *PLoS One* 9 (2014) e109136.

Chapter 2. Structural Comparison of Group 12 Complexes of a Tripodal Mixed NS(thiolato) Donor Ligand

1. Introduction

Distribution of amino acid side chain contacts in the protein database suggest that Zn^{2+} , Cd^{2+} , and Hg^{2+} share a common preference for cysteine and histidine ligation [1]. Furthermore, these amino acids appear together in a variety of group 12 metal ion protein binding sites. For example, His_2Cys_2 zinc fingers are common structural components of enzymes [2]. Evidence for histidine metal bonding has also recently been reported for several cysteine-rich metallothioneins, proteins with functions ranging from zinc homeostasis to Cd^{2+} and Hg^{2+} detoxification [3]. Zinc centers with both histidine and cysteine ligation in proteins span catalytic sites in all six enzyme classes (Table 1) and regulatory sites in at least three enzyme classes (Table 2) [4]. Significantly, the cambialistic ζ -class of carbonic anhydrases from marine diatoms relying on Cd^{2+} as their metal cofactor when Zn^{2+} is scarce have His_2Cys metal binding environments like the β -class of Zn^{2+} -dependent carbonic anhydrase instead of the His_3 associated with most Zn^{2+} -dependent classes [5].

Table 1. Representative proteins containing catalytic Zn²⁺-cysteine-histidine complexes.

Enzyme Class	Protein	Zn ²⁺ -sidechain interactions	PDB
Oxidoreductase	Alcohol dehydrogenase	Cys44, His66, Glu167 & Cys173	1MC5 [6]
	Sorbitol dehydrogenase	Cys 44, His69 & Glu 70	1PL7 [7]
Transferase	RING-type E3 ubiquitin transferase	Cys100, Cys103, His115& Cys119; Cys52, His54, Cys72, Cys 75	5DKA [8]
	Protein farnesyltransferase	Asp297, Cys299 & His362 (β-subunit)	1JCQ [9]
Hydrolase	Cytidine deaminase	His67, Glu69, Cys101 & Cys106	2KEM [10]
	Peptide Deformylase	Cys90, His132 & His136	1DFF [11]
	GTP Cyclohydrolase I	Cys141, Cys212 & His143	1FB1 [12]
Lyase	Aprataxin and PNK-like factor	Cys379, Cys385, His392 & His398; Cys421, Cys427, His434 & His440	2KQB [13]
Isomerase	Peptidyl-prolyl cis-trans isomerase FKBP1B	Cys4611, Cys4608 & His4628	6PV6 [14]
Ligase	Threonyl-tRNA Synthetase	Cys105, His156 & His282	4P3N [15]

Adapted from Reference [4]

Table 2. Representative proteins containing regulatory Zn²⁺-cysteine-histidine complexes.

Enzyme Class	Protein	Zn ²⁺ -sidechain interactions	PDB
Hydrolase	Dimethylarginine dimethylaminohydrolase	His172, Cys273, Glu77 & Asp78	2CI7 [16]
Kinase	Protein kinase C	His102, His140, Cys115, Cys118, Cys132, Cys135, Cys143 & Cys151	3PFQ [17]
Protease	Caspase-9	His237, Cys239 & Cys287	1JXQ [18]
	Cathepsin S	Cys25 & His164	2HH5 [19]

Adapted from Reference [4]

Despite the concurrence of histidine and cysteine in the active sites of proteins associated with group 12, coordination studies of these metal ions with chelating ligands containing a combination of aromatic amine and alkylthiolate ($N_x^A S_y^-$) donors have been rare. A search of the Cambridge Crystallographic Database [20] reveals two Cd^{2+} complexes [21,22] and two Hg^{2+} complexes [22,23] involving chelating $N_x^A S_y^-$ ligands. Interestingly, a study inspired by the metal-promiscuity of metallothionein used a $N_x^A S_y^-$ ligand to provide the first crystallographically characterized complexes containing both Zn^{2+} and Hg^{2+} bound to the same ligand [24]. A limited variety of bi-, tri- and tetradentate $N_x^A S_y^-$ ligands have been used to prepare structurally characterized Zn^{2+} complexes [20].

The tripodal ligand 2-[bis(2-pyridinylmethyl)amino]ethanethiol (**L1H**; Figure 1) was chosen for this study because it has supported preparation of small molecule models of cysteine- and histidine-containing protein metal binding sites. A complex of **L1** with bis(μ -thiolato)dicopper(II) core resembles the Cu_A sites of cytochrome *c* oxidase and nitrous oxide reductase [25]. In addition, the mononuclear trigonal bipyramidal complex $[Zn(\mathbf{L1})Cl]$ was found to promote metallo- β -lactamase-like hydrolysis activity [26]. The rate of bis(*p*-nitrophenyl)hydrogen phosphate hydrolysis increased linearly with $[Zn(\mathbf{L1})Cl]$ at low concentrations, but gradually decreased at higher concentration suggesting a monomer-dimer equilibrium. Adding methyl groups ortho to the pyridyl nitrogen of **L1H** produced a similar mononuclear square pyramidal complex [27]. In this section, the syntheses, X-ray crystallography, XPRD, 1H NMR, and IR of

[Cd(**L1**)Cl]₂·benzene (**1**) and [Hg(**L1**)Cl] (**2**) are described, completing the first series of group 12 complexes with a common chelating N^AS⁻_y ligand.

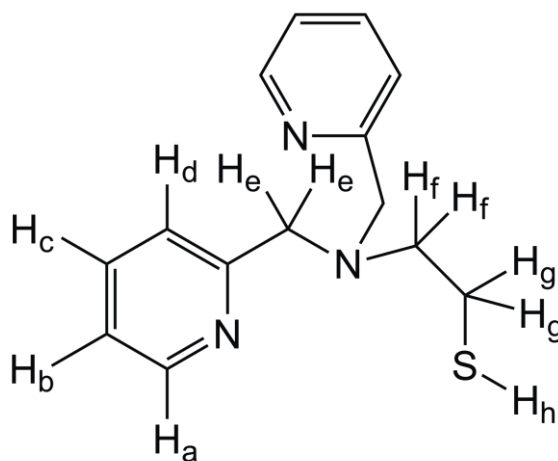


Figure 1. Structure of **L1H** with proton labels.

2. Experimental

2.1 Reagents and Methods

Organic solvents and reagents were of commercial grade and used as received. Metal salts were dried under vacuum overnight. Elemental analyses were carried out by Atlantic Microlab, Inc., Norcross, Georgia. Capillary melting points were obtained using a Mel-Temp apparatus and are uncorrected. ^1H NMR spectra were collected in 5 mm o.d. NMR tubes on a Agilent 400MR DD2 NMR spectrometer. IR spectra were collected on a Digital Labs FTS 7000 using a diamond ATR probe.

X-ray diffraction data were collected on a Bruker AXS Apex DUO three-circle diffractometer system with a graphite monochromator, SMART APEX II CCD detector using φ and ω scans, and a Mo $K\alpha$ fine-focus sealed tube ($\lambda = 0.71073$ Å). Selected crystallographic data are given in Tables 3 and 4. The structures were solved by direct methods and refined on F^2 by full-matrix least squares using the ShelXle program package. All non-hydrogen atoms were refined anisotropically and the hydrogens were placed theoretically.

*2.2 Synthesis of **L1H***

L1H was synthesized and purified by literature methods [26]. ^1H NMR (CD_3CN , 20 °C): ^1H NMR (CDCl_3) δ 8.506 (d, 4 H, $J = 5.0$ Hz, H_a), 7.643 (dt, 4 H, $J = 1.9, 7.8$ Hz, H_c), 7.519 (d, 4 H, $J = 7.8$ Hz, H_d), 7.139 (d, 4 H, $J = 5.3, 7.4$ Hz, H_b), 3.829 (s, 4 H, H_e), 2.792 (m, 4 H, H_g), 2.652 (m, 4 H, H_i); (CD_3CN) δ 8.478 (d, 4 H, $J = 5.1$ Hz, H_a), 7.708 (dt, 4 H, $J = 1.7, 7.8$ Hz, H_c), 7.547 (d, 4 H, $J = 7.7$ Hz, H_d), 7.199

(d, 4 H, $J = 4.9, 7.6$ Hz, H_b), 3.784 (s, 4 H, H_e), 2.730 (m, 4 H, H_g), 2.648 (m, 4 H, H_f).

2.3 Synthesis of $[Cd(L1)Cl]_2 \cdot benzene$ (**1**)

One equivalent of CdCl₂ (58 mg, 316 μ mol) was dissolved in a solution of KOH (0.4 M in MeOH, 790 μ L, 316 μ mol) and **L1H** (82 mg, 316 μ mol) in 22 mL methanol by stirring overnight. Benzene was added dropwise to the cloud point. After clarifying with methanol, the pale yellow solution was filtered through Celite and set aside for slow evaporation. Colorless X-ray quality crystals of **1** (27 mg, 19% yield) formed over a month. MP: 232 – 235 °C. ¹H NMR (CD₃CN, saturated (< 2 mM), 20 °C): δ 8.904 (d, 4 H, $J = 4.9$ Hz, H_a), 7.931 (ddd, 4 H, $J = 1.7, 7.8, 7.8$ Hz, H_c), 7.504 (dd, 4 H, $J = 5.0, 7.6$ Hz, H_b), 7.420 (d, 4 H, $J = 6.8$ Hz, H_d), 7.371 (s, 6 H, H_{benzene}), 3.999 (d, 4 H, $J = 15.4$ Hz, H_e), 3.749 (d, 4 H, $J = 15.5$ Hz, H_{e'}), 2.760-2.660 (m, 4 H, H_{f,g}). IR (ATR) ν/cm^{-1} : 617(w), 633(w), 646(w), 660(w), 689(s), 723(w), 768(s), 802 (w), 825(w), 845(w), 920(w), 935(w), 966(w), 988(w), 1011(m), 1036(w), 1051(w), 1096(m), 1121(w), 1150(m), 1217(w), 1260(w), 1275(w), 1292(w), 1304(w), 1348(w), 1389(w), 1431(m), 1458(w), 1476(m), 1572(w), 1595(m), 2342(w), 2363(w), 2843(w), 2909(w). Anal. Calc for vacuum dried (benzene lost) $2C_{28}H_{32}CdCl_2N_6S_2$: 45.85 C, 4.30 H, 9.44 N. Found: 45.96 C, 4.28 H, 9.42 N.

2.4 Synthesis of $[Hg(L1)Cl]$ (**2**)

One equivalent of NaOH in methanol (0.4 M, 235 μ L, 94 μ mol) was added to a solution of **L1H** (60.9 mg, 235 μ mol) in 1.5 mL methanol and HgCl₂ (63.8 mg, 235 μ mol) in 3 mL methanol. Triethylamine was added dropwise to the cloud point,

followed by dropwise addition of acetonitrile to clarify. The solution was filtered through Celite and set aside. After seven days, the clear solution was carefully decanted from trace gray sediment and set aside for slow evaporation. Colorless X-ray quality crystal (62.2 mg, 53.5% yield) were obtained a week later. DP: 118 °C. ^1H NMR (CD_3CN , nominally 2 mM, 20 °C) δ : 8.873 (d, 2H, J = 5.0 Hz, H_a), 7.831 (ddd, 2H, J = 1.8, 7.7, 7.7 Hz, H_c), 7.417 (dd, 2H, J = 5.1, 8.2 Hz, H_b), 7.358 (d, 2H, J = 7.2 Hz, H_d), 3.810 (bs, 4H, H_e), 2.875 (bs, 2H, H_g), 2.695 (m, 2H, H_f). IR (ATR) ν/cm^{-1} : 633(m), 644(w), 660(w), 687(w), 723(m), 760(s), 802(w), 837(w), 891(m), 912(w), 939(w), 962(w), 988(w), 1009(m), 1026(w), 1049(m), 1092(m), 1109(w), 1128(m), 1155(w), 1196(w), 1236(w), 1265(m), 1285(w), 1300(w), 1315(w), 1371(m), 1435(s), 1472(m), 1573(m), 1597(s), 2835(w), 2878(w), 2914(w), 2940(w), 3742(w), 3750(w), 3852(w). Anal. Calc for $\text{C}_{14}\text{H}_{16}\text{ClHgN}_3\text{S}$: 34.01 C, 3.26 H, 8.50 N. Found: 34.06 C, 3.22 H, 8.49 N.

Table 3. Crystallographic data for [Cd(L1)Cl]₂·benzene (1) and [Hg(L1)Cl] (2)

	[Cd ₂ (L1) ₂ Cl ₂]·benzene	[Hg(L1)Cl]
Empirical Formula	C ₃₄ H ₃₈ Cd ₂ Cl ₂ N ₆ S ₂	C ₁₄ H ₁₆ ClHgN ₃ S
Formula mass [g mol ⁻¹]	890.52	494.40
Crystal Size [mm ³]	0.30 × 0.45 × 0.58	0.12 × 0.48 × 0.48
Crystal System	Triclinic	Monoclinic
Space Group	<i>P</i> -1	<i>P</i> 2 ₁ / <i>c</i>
<i>a</i> [Å]	9.0044(9)	12.5678(13)
<i>b</i> [Å]	10.0424(10)	7.6751(8)
<i>c</i> [Å]	10.5406(10)	16.4006(18)
α[°]	75.097(2)	90
β[°]	72.253(2)	96.284
γ[°]	88.380(2)	90
<i>V</i> [Å ³]	875.95(15)	1572.5(3)
<i>Z</i>	1	4
Radiation (monochromatic)	Mo <i>K</i> α	Mo <i>K</i> α
<i>T</i> [K]	103(2)	103(2)
ρ _{calc} [Mg m ⁻³]	1.688	2.088
λ [Å]	0.71073 Å	0.71073 Å
μ [mm ⁻¹]	1.520	10.083
Measured reflections	6818	11184
Ind. Reflections [<i>R</i> _(int)]	4138 [0.0303]	3746[0.0423]
Completeness to θ = 28.29°	95.3 %	95.1%
Data / restraints / parameters	4138 / 0 / 209	3726/0/182
<i>R</i> 1 ^{<i>a</i>} , <i>wR</i> 2 ^{<i>b</i>} [<i>I</i> > 2σ(<i>I</i>)]	0.0269, 0.0742	0.0275, 0.0579
<i>R</i> 1 ^{<i>a</i>} , <i>wR</i> 2 ^{<i>b</i>} (all data)	0.0276, 0.0748	0.0324, 0.0594
Goodness-of-fit (GOF)	1.062	1.105
<i>T</i>	N/A	0.44

Table 4. Selected bond lengths and angles for [M(L1)Cl]_n

M n	Cd 1	Hg 2	Zn (Kurosaki 2000) 3
M–N1A	2.4122(17)	2.510(4)	2.113(3)
M–N1B	2.4394(18)	2.480(3)	2.130(4)
M–N	2.4753(17)	2.644(3)	2.313(3)
M–S	2.6777(5)	2.4185(12)	2.303(1)
M–Cl	2.5264(6)	2.4591(11)	2.337(1)
M–S#1	2.6449(6)		
N1A–M–N1B	84.66(6)	103.22(12)	115.0(1)
N1A–M–N	68.76(6)	67.43(11)	75.6(1)
N1B–M–N	71.17(6)	66.65(11)	76.1(1)
N1A–M–Cl	91.85(4)	91.60(9)	98.6(1)
N1B–M–Cl	92.30(5)	93.22(9)	97.0(1)
N–M–Cl	155.12(4)	144.96(8)	167.59(9)
N1A–M–S	148.82(4)	110.88(9)	118.68(10)
N1B–M–S	85.14(4)	118.68(9)	116.0(1)
N–M–S	80.05(4)	81.47(8)	85.80(9)
Cl–M–S	117.952(18)	133.34(4)	106.57(5)
N1B–M–S#1	165.58(5)		
N1A–M–S#1	95.18(4)		
N–M–S#1	95.29(4)		
Cl–M–S#1	102.108(19)		

3. Results and Discussion

3.1 Synthesis of **1** and **2**

New compounds of Cd and Hg with the N₃S donor ligand **L1** were prepared by self-assembly in methanol solutions containing one equivalent of **L1** per equivalent of metal chloride. Colorless crystals of [Cd(**L1**)Cl]₂·benzene were obtained in low yield by slow evaporation using benzene as a co-solvent. The complex had a satisfactory elemental analysis allowing for the loss of benzene during vacuum drying. Colorless crystals of [Hg(**L1**)Cl] were obtained by slow evaporation using triethylamine as a co-solvent. After separation from an initial grey precipitate, slow evaporation of the mother liquor provided X-ray quality crystals with satisfactory elemental analysis. Both compounds were characterized by X-ray diffraction and variable temperature ¹H NMR.

3.2 Structure of [Cd(**L1**)Cl]₂·benzene

The neutral dinuclear complex [Cd(**L1**)Cl]₂·benzene (**1**) crystallized by slow evaporation from methanol/benzene in the triclinic space group *P*-1 with one dimeric complex and well-ordered benzene molecule per unit cell. Both the complex and the benzene molecule lie on crystallographic inversion centers. As shown in Figure 2, each metal center has distorted octahedral ClN₃S₂ coordination provided by a tetradentate **L1**, a terminal chloride and a bridging thiolate from the ligand bound to the other metal ion. The N1B pyridyl nitrogens are trans to chelating thiolate sulfurs and the N1A pyridyl nitrogens are trans to bridging thiolate sulfurs. Finally, the tertiary amine nitrogen and chloride are trans and located on either side of the plane containing the (CdS)₂ ring.

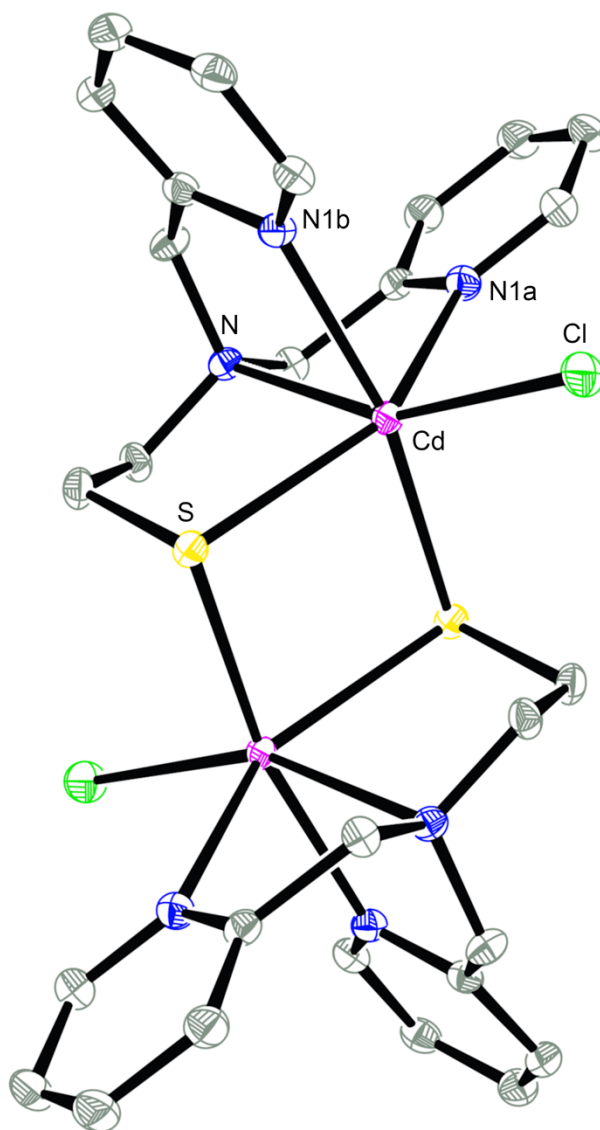


Figure 2. Thermal ellipsoid (50% probability) structure of $[\text{Cd}(\text{L1})\text{Cl}]_2 \cdot \text{benzene}$ (**1**). Hydrogen atoms and benzene solvent molecules are omitted for clarity.

The chelating Cd–S bond lengths (2.6777(5) Å) are slightly longer than the bridging ones (2.6449(6) Å). The average Cd–N_{pyr} bond length is 2.4258(18) Å, somewhat shorter than the Cd–N_{am} bond length (2.4753(17) Å). The N1A and S chelate ring have envelope conformations with the aliphatic nitrogen and adjacent methylene carbon in the flap positions, respectively. In contrast, the N1B chelate

ring has a half chair conformation. Geometric constraints of the tripodal ligand likely cause displacement of the metal ion from the N1A–N1B–S–S#1 plane towards the chloride, resulting in many distortions from regular octahedral geometry. In addition, torsional strain between substituents on the planar (CdS)₂ ring is moderated by the 155.12(4)° Cl–Cd–N bond angle.

The supramolecular structures of **1** is stabilized through synergistic offset face-to-face π – π (OFF) and edge-to-face π – σ (EF) aromatic interactions. The dimer complex is assembled into sheets through OFF between pairs of N1A pyridyl rings and pairs of N1B pyridyl rings (Fig. 3). The lattice benzene is anchored through cooperative EF interactions with four N1A pyridyls (Fig. 3). Benzene placement in channels between sheets is consistent with the ready solvent loss under vacuum (Fig. 4). No hydrogen bonding interactions were observed.

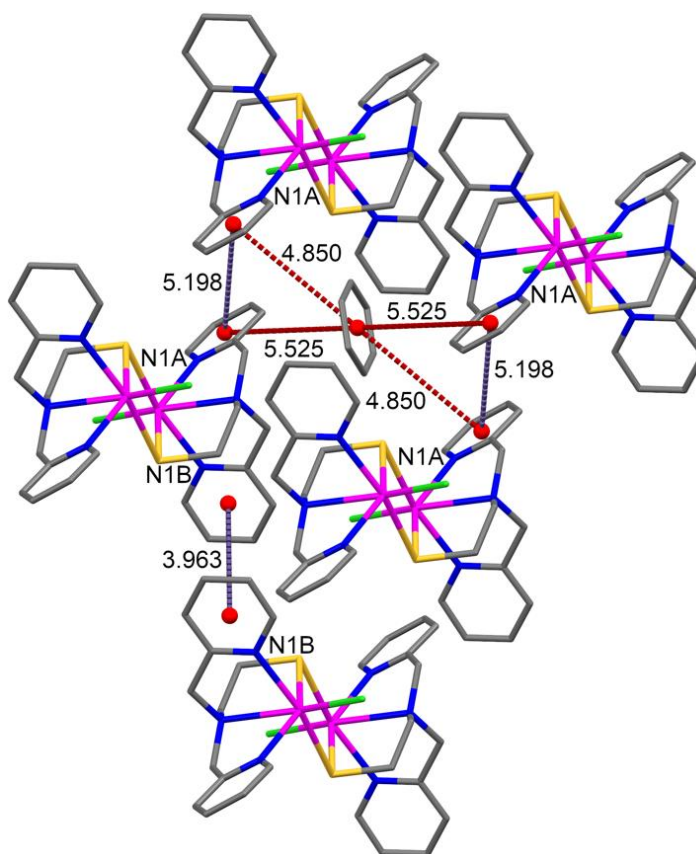


Figure 3. Intermolecular aromatic stacking interactions between pyridyl rings identified by their nitrogen atom and benzene trapped in the crystal lattice of **1**. Hydrogen atoms are omitted for clarity.

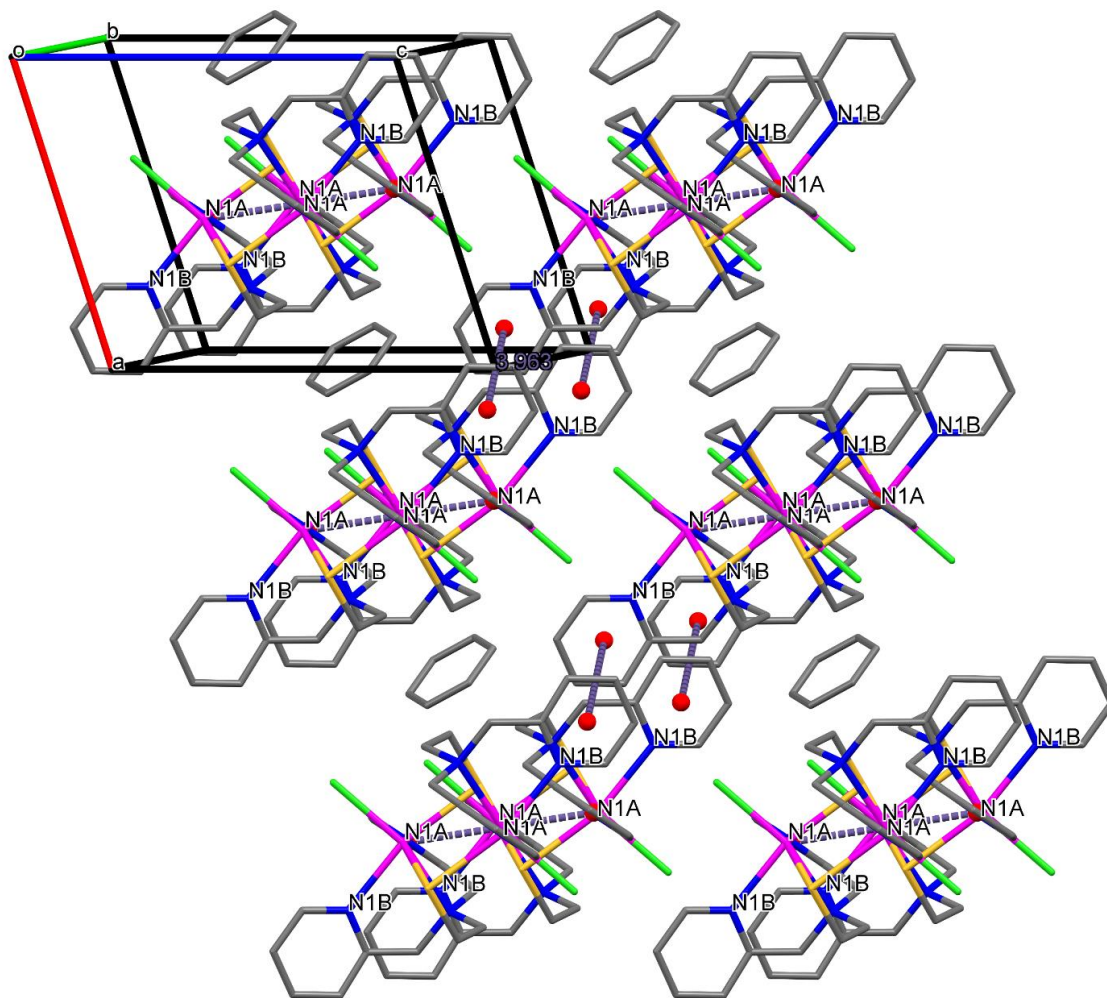


Figure 4. Packing diagram of **1** along b^* showing formation of sheets through pairwise N1A pyridyl and N1B pyridyl OFF interactions. Benzene molecules held in place by EF with N1A pyridyl rings are located between sheets.

3.3 Structure of $[\text{Hg}(\text{L1})\text{Cl}]$

The neutral mononuclear complex $[\text{Hg}(\text{L1})\text{Cl}]$ (**2**) crystallized by slow evaporation from acetonitrile in the monoclinic space group $P2_1/c$ with four molecules per unit cell. As shown in Figure 5, the metal has ClN_3S coordination. Complex **2** has mixed coordination geometry ($\tau = 0.44$) with predominantly square pyramidal character.

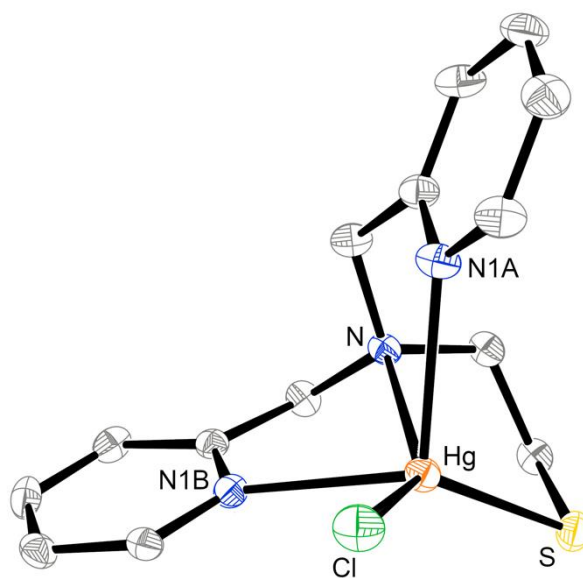


Figure 5. Thermal ellipsoid (50% probability) structure of $[\text{Hg}(\text{L1})\text{Cl}]$ (**2**). Hydrogen atoms are omitted.

For the nominally axial pyridyl nitrogen N1A the bond distance to the metal center (2.510(4) Å) is slightly longer than its nominally equatorial counterpart N1B (2.480(3) Å). The Hg–N bond distance to the tripodal ammine nitrogen is longer (2.644(3) Å) than the Hg–N bonds to both pyridyl nitrogens as observed in **1**. The N1A chelate ring has an envelope conformation with the methylene carbons in the flap positions. Both the N1B and S chelate ring have a half chair conformation. The mercury is within 0.280 Å of the N–N1b–Cl–S square plane.

The supramolecular structure of **2** is extensively stabilized through interactions between aromatic rings (Figure 6). Both pyridyl rings undergo OFF with their counterparts in inversion related neighboring molecules. In addition, EF interactions occur between the N1A and N1B pyridyls of neighboring inversion related molecules. These interactions form continuous chains of the complex along

the *a* cell axis. These chains are linked into a three-dimensional network through EF interactions between the N1A pyridyls that extend along two-fold screw axes.

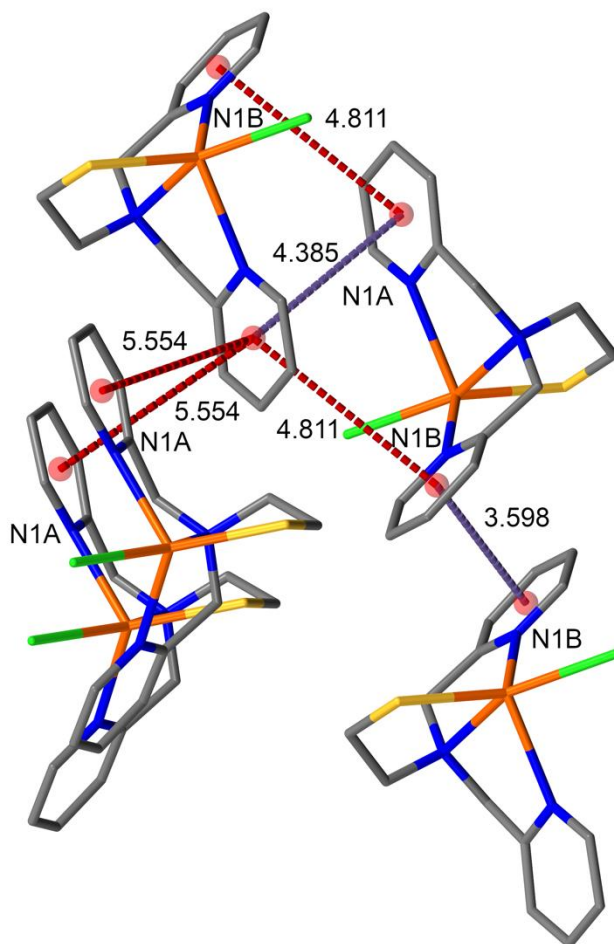


Figure 6. Intermolecular aromatic stacking interactions between pyridyl rings, identified by their nitrogen atoms, in **2**. Hydrogen atoms are omitted for clarity. OFF in violet; EF in red.

3.4 Structural Comparison of Group 12 $[M(\mathbf{L1})\text{Cl}]_n$ Complexes

Known complex $[\text{Zn}(\mathbf{L1})\text{Cl}]$ (**3**) [26] crystallized in $P2_1/c$ as an isomorph of **2**. Although **3** has a predominantly trigonal bipyramidal structure ($\tau = 0.82$), it overlays well with the structure of **2** (Fig. 7) and has a similar network of pi stacking interactions (Figure 8). Consistent with the smaller ionic radius of Zn^{2+} , the metal

ligand bond distances in **3** are all shorter than those in **1** and **2**. The N–M–Cl bond angle is the largest around the metal ion in all three complexes and closest to the ideal value of 180° in **3**. The Cl–M–S bond angle is larger than the 90° ideal for all three complexes and the only metal bond angle that increases as the metal ion gets larger.

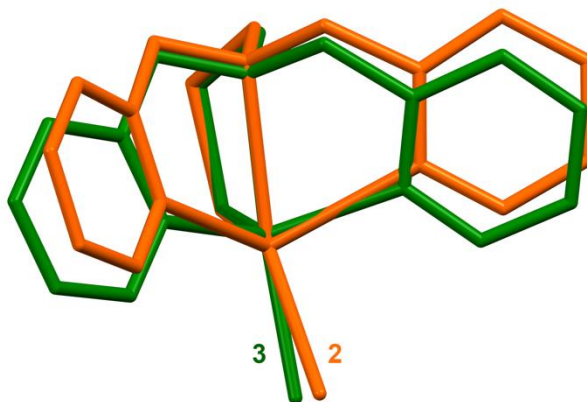


Figure 7. Overlay diagram (N–M–S) for isomorphs **2** and **3**.

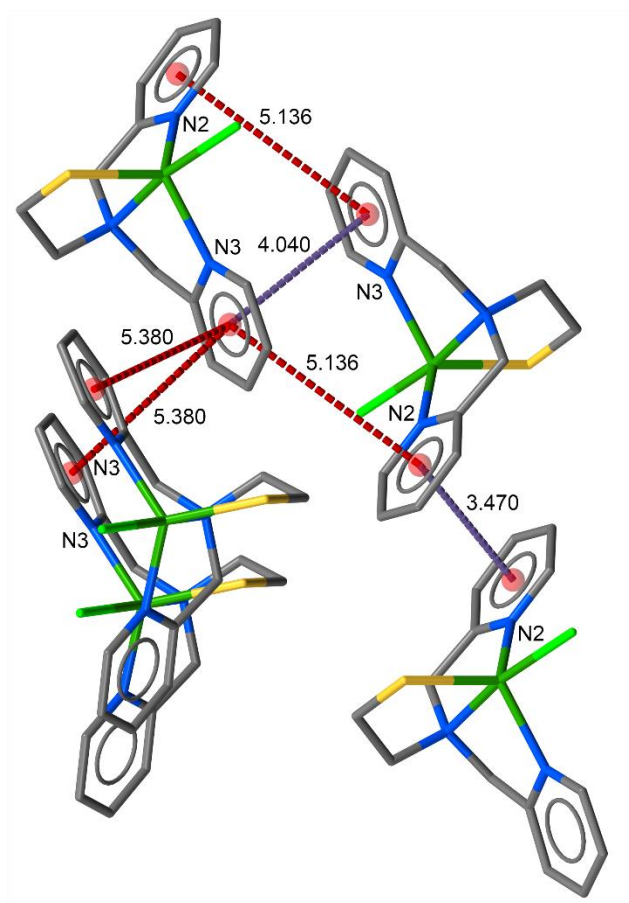


Figure 8. Intermolecular aromatic stacking interactions between pyridyl rings, identified by their nitrogen atoms, in **3** (CDC Refcode XALTEJ) [26]. Hydrogen atoms are omitted for clarity. OFF in violet; EF in red.

3.5 Proton NMR of **1** and **2**

Proton NMR spectra were obtained for both **1** (saturated < 3 mM) and **2** (nominally 0.6–5.0 mM) in CD₃CN solutions over the temperature range –40 °C to 20 °C. Correlations between solid-state structures and solution-state spectroscopy are rarely definitive for group 12 metal ion complexes due to intramolecular reorganization, intermolecular exchange and variable oligomerization. However, temperature and concentration studies can be enlightening when broadened resonances are observed. Both **1** and **2** had a single set of ligand proton

resonances at the concentrations examined. The pyridyl rings of **1** have structurally distinct locations trans from either the intraligand or bridging thiolate which are not magnetically equivalent. Significantly, the proton NMR of **1** had both geminal ^1H - ^1H coupling and small $J(^{111/113}\text{Cd}^1\text{H})$ couplings (Fig. 9; comparable coupling at 20 °C) providing definitive evidence for slow intermolecular metal-ligand exchange on the coupling constant time scale. Magnetic equivalence of the pyridyl rings of **1** can be explained by the coordinative malleability of the d^{10} metal ion allowing for rapid intramolecular exchange of the thiolate positions in the Cd_2S_2 ring without bond cleavage (Fig. 9.5). Although **2** has two unique pyridyls in the solid-state structure, pyridyl equivalence would be expected for the mononuclear complex after removal of solid-state constraints. Unlike **1**, cryogenic conditions were required to observe heteronuclear coupling between the metal ion and ligand protons of **2**. The four pyridyl proton resonances had similar chemical shifts for the two complexes ($\Delta\delta \leq 0.10$ ppm) and exhibited only a modest linear dependence on temperature and negligible changes with concentration.

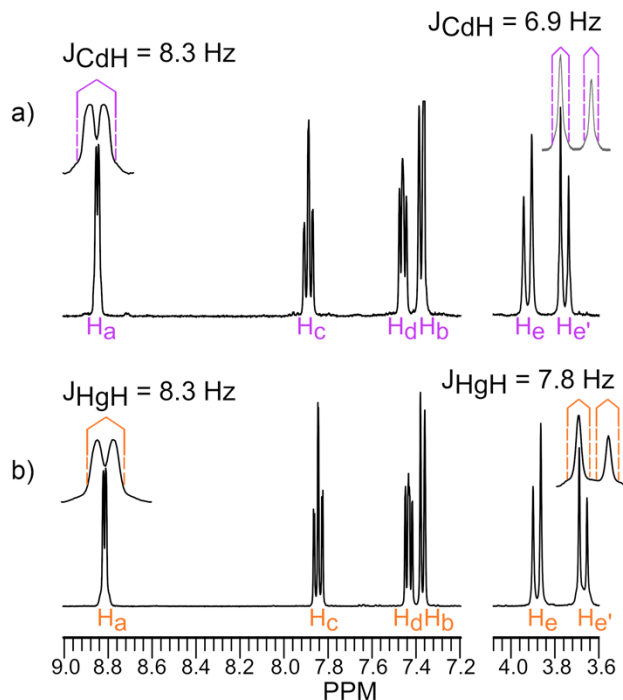


Figure 9. ^1H NMR highlights (CD_3CN , nominally 2 mM, -40°C) for a) $[\text{Cd}(\text{L1})\text{Cl}]_2 \cdot \text{benzene}$ and b) $[\text{Hg}(\text{L1})\text{Cl}]$. Heteronuclear $J(^{111/113}\text{Cd}^1\text{H})$ and $J(^{199}\text{Hg}^1\text{H})$ couplings are shown as insets. Multiplets for H_f and H_g between 2.66 and 2.90 ppm not shown.

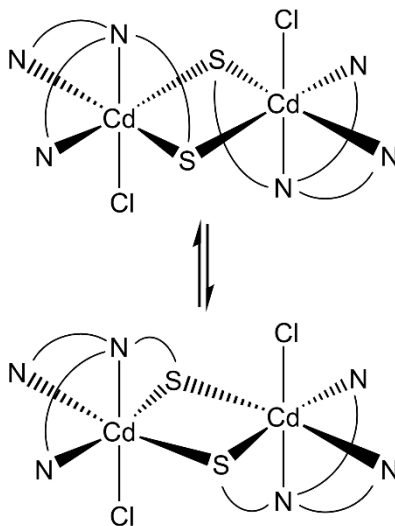


Figure 9.5. Proposed intramolecular twist for exchange of the thiolate positions in the Cd_2S_2 ring and associated pyridyl environments.

While the pyridyl protons of **1** and **2** exhibited similar behavior, the aliphatic protons behaved differently as a function of temperature. Geminally coupled methylene proton peaks were observed for **1**, and the more upfield H_e protons had $J(^{111/113}\text{Cd}^1\text{H})$ satellites, over the temperature range $-40\text{ }^{\circ}\text{C}$ to $20\text{ }^{\circ}\text{C}$. For **2**, at $-40\text{ }^{\circ}\text{C}$ the methylene protons were geminally coupled, with $J(^{199}\text{Hg}^1\text{H})$ satellites around the more shielded H_e, but these couplings were lost and the methylene resonances coalesced into a singlet as the temperature was increased (Fig. 10). Significantly, the coalescence of the methylene peaks coincided with the coalescence of major and minor (12%) peaks for H_g with $\Delta\delta$ 0.18 ppm and essentially no changes to the rest of the spectrum (Fig. 10). Furthermore, serial dilution of the sample partially resolved the methylene protons, indicating an intermolecular process was occurring and supporting assignment of the major species to mononuclear ligand complex **2** (Fig. 11). These spectral changes are potentially associated with an equilibrium between **2** and a variety of dimers (Fig. 12). The initially formed μ -thiolato-bridged dimer **7** is proposed to undergo rapid association-assisted Hg–S bond cleavage (**8**), followed by nitrogen inversion to exchange the methylene proton environments (**8'**), reformation of the Hg–S bond (**7'**) and dissociation back to monomers at higher temperatures and concentrations. Under conditions in which Hg–S bond dissociation is slow, bis- μ -thiolato dimer **9** is proposed to form by reorganization of the initial μ -thiolato-bridged dimer and ring closure, giving rise to the minor chemical shift environment for H_g (Fig. 12). Dimerization is expected to have a higher impact on the H_f and H_g protons closer to the dimerization interface as observed. Chemical shift differences

for more distant protons are likely too modest for detection by broadening on the chemical shift time scale under accessible conditions. Transient cleavage of the Hg–N is plausible, but considered less likely due to the invariance of the pyridyl region of the ^1H NMR spectrum. The $[\text{Zn}(\text{L1})\text{Cl}]$ complex was also suggested to undergo a monomer-dimer equilibrium [26].

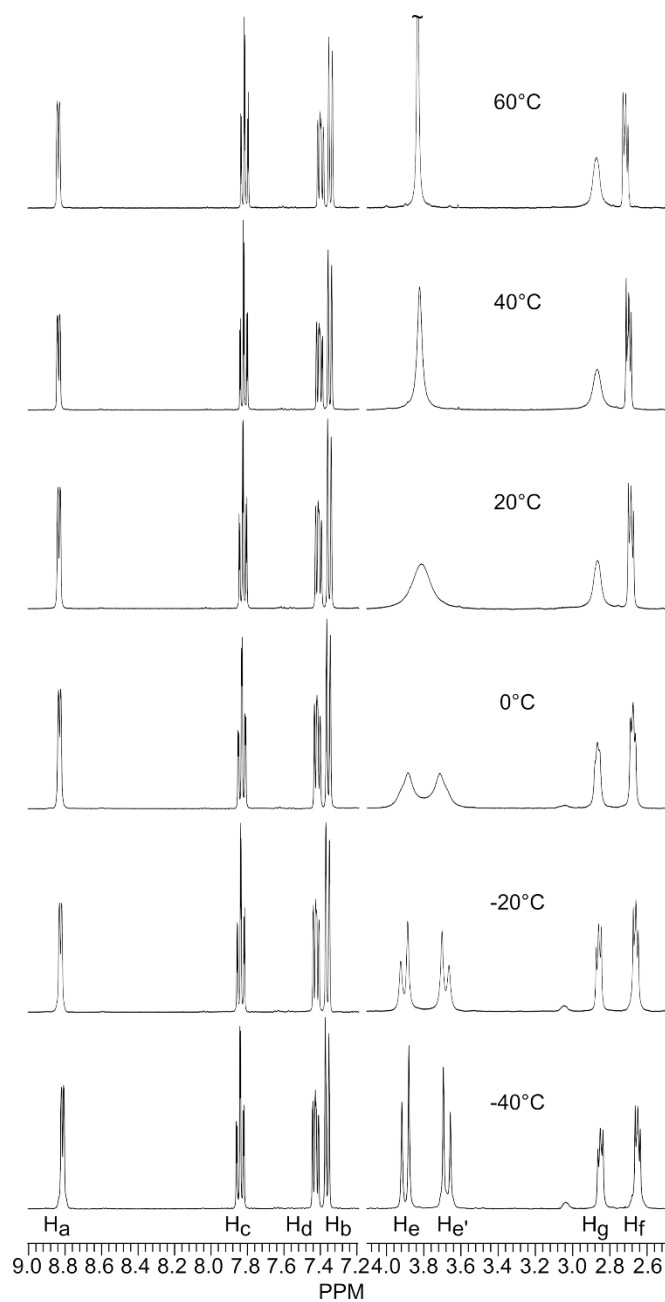


Figure 10. Ligand proton resonances for **2** (CD_3CN , nominally 5 mM) as a function of temperature.

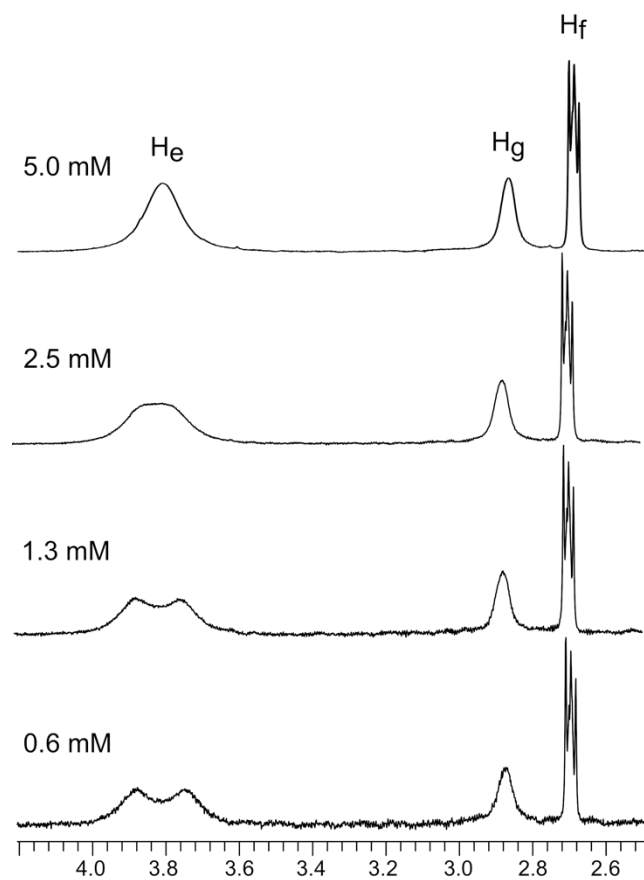


Figure 11. Methylene and ethylene proton resonances for **2** in CD_3CN solution at 20°C as a function of nominal solution concentration.

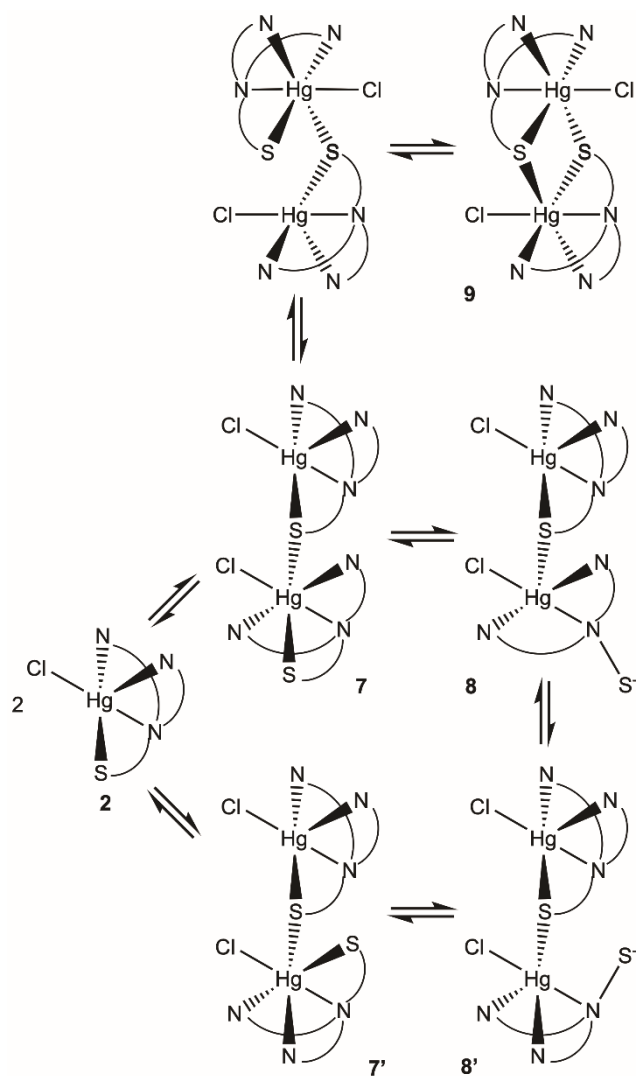


Figure 12. Proposed pathway for dynamic processes involving **2**. Primes added to compound numbers to indicate inversion of the central amine and exchange of methylene proton environments.

4. Conclusion

New chloride complexes of Cd^{2+} and Hg^{2+} with the deprotonated N_3S donor ligand 2-[bis(2-pyridinylmethyl)amino]ethanethiol (**L1H**) were synthesized and characterized in both the solid state and solution state for comparison with the known complex $[\text{Zn}(\text{L1})\text{Cl}]$. The dinuclear cadmium complex crystallized as $[\text{Cd}(\text{L1})\text{Cl}]_2 \cdot \text{benzene}$ in the triclinic space group $P\bar{1}$ with an octahedral Cd^{2+} coordination geometry. The two metal centers of the dimeric complex are bridged by ligand thiolate groups. Mononuclear $[\text{Hg}(\text{L1})\text{Cl}]$ crystallized in the monoclinic space group $P2_1/c$ with mixed pyramidal/trigonal bipyramidal geometry ($\tau = 0.44$) as an isomorph of the predominantly trigonal bipyramidal complex **3**. Variable temperature and variable concentration proton NMR of $[\text{Hg}(\text{L1})\text{Cl}]$ suggested a possible equilibrium between the dimer and monomer form in solution at high temperature and low concentration. A similar equilibrium was also suggested for $[\text{Zn}(\text{L1})\text{Cl}]$. In contrast, the proton NMR of $[\text{Cd}(\text{L1})\text{Cl}]_2 \cdot \text{benzene}$ did not exhibit broadening or variations suggesting negligible dimer-monomer equilibrium over the same concentration and temperature range.

References

- [1] R Friedman. Structural and computational insights into the versatility of cadmium binding to proteins, *Dalton Trans.* 43 (2014) 2878–2887.
- [2] SV Razin, VV Borunova, OG Maksimenko, OL Kantidze. Cys₂His₂ zinc finger protein family: Classification, functions, and major members, *Biochem. (Mosc.)* 77 (2012) 217–226.
- [3] M Perinelli, M Tegoni, E Freisinger. Different Behavior of the Histidine Residue toward Cadmium and Zinc in a Cadmium-Specific Metallothionein from an Aquatic Fungus, *Inorg.Chem.* 59 (2020) 16988–16997.
- [4] NJ Pace, E Weerapana. Zinc-binding cysteines: diverse functions and structural motifs, *Biomolecules* 4 (2014) 419–434.
- [5] V Alterio, E Langella, G De Simone, SM Monti. Cadmium-Containing Carbonic Anhydrase CDCA1 in Marine Diatom *Thalassiosira weissflogii*, *Mar. Drugs* 13 (2015) 1688–1697.
- [6] PC Sanghani, WF Bosron, TD Hurley. Human glutathione-dependent formaldehyde dehydrogenase. Structural changes associated with ternary complex formation, *Biochem.* 41 (2002) 15189–15194.
- [7] TA Pauly, JL Ekstrom, DA Beebe, B Chrnyk, D Cunningham, M Griffor, A Kamath, SE Lee, R Madura, D Mcguire. X-ray crystallographic and kinetic studies of human sorbitol dehydrogenase, *Structure* 11 (2003) 1071–1085.
- [8] M Bijlmakers, JMC Teixeira, R Boer, M Mayzel, P Puig-Sàrries, G Karlsson, M Coll, M Pons, B Crosas. A C₂HC zinc finger is essential for the RING-E2 interaction of the ubiquitin ligase RNF125, *Sci. Rep.* 6 (2016) 29232.
- [9] SB Long, PJ Hancock, AM Kral, HW Hellinga, LS Beese. The crystal structure of human protein farnesyltransferase reveals the basis for inhibition by CaaX tetrapeptides and their mimetics, *Proc. Natl. Acad. Sci. U.S.A.* 98 (2001) 12948–12953.
- [10] E Harjes, PJ Gross, K Chen, Y Lu, K Shindo, R Nowarski, JD Gross, M Kotler, RS Harris, H Matsuo. An extended structure of the APOBEC3G catalytic domain suggests a unique holoenzyme model, *J.Mol.Biol.* 389 (2009) 819–832.
- [11] MK Chan, W Gong, PR Rajagopalan, B Hao, CM Tsai, D Pei. Crystal structure of the *Escherichia coli* peptide deformylase, *Biochemistry (N.Y.)* 36 (1997) 13904–13909.

- [12] G Auerbach, A Herrmann, A Bracher, G Bader, M Gütlich, M Fischer, M Neukamm, M Garrido-Franco, J Richardson, H Nar. Zinc plays a key role in human and bacterial GTP cyclohydrolase I, *Proc. Natl. Acad. Sci. U.S.A.* 97 (2000) 13567–13572.
- [13] S Eustermann, C Brockmann, PV Mehrotra, J Yang, D Loakes, SC West, I Ahel, D Neuhaus. Solution structures of the two PBZ domains from human APLF and their interaction with poly(ADP-ribose), *Nat. Struct. Mol. Biol.* 17 (2010) 241–243.
- [14] A Dashti, G Mashayekhi, M Shekhar, D Ben Hail, S Salah, P Schwander, A des Georges, A Singharoy, J Frank, A Ourmazd. Retrieving functional pathways of biomolecules from single-particle snapshots, *Nat. Commun* 11 (2020) 4734.
- [15] P Fang, X Yu, SJ Jeong, A Mirando, K Chen, X Chen, S Kim, CS Francklyn, M Guo. Structural basis for full-spectrum inhibition of translational functions on a tRNA synthetase, *Nat. Commun* 6 (2015) 6402.
- [16] D Frey, O Braun, C Briand, M Vašák, MG Grütter. Structure of the mammalian NOS regulator dimethylarginine dimethylaminohydrolase: A basis for the design of specific inhibitors, *Structure* 14 (2006) 901–911.
- [17] TA Leonard, B Różycki, LF Saidi, G Hummer, JH Hurley. Crystal structure and allosteric activation of protein kinase C β II, *Cell* 144 (2011) 55–66.
- [18] KL Huber, JA Hardy. Mechanism of zinc-mediated inhibition of caspase-9, *Protein Sci.* 21 (2012) 1056–1065.
- [19] DC Tully, H Liu, AK Chatterjee, PB Alper, R Epple, JA Williams, MJ Roberts, DH Woodmansee, BT Masick, C Tumanut. Synthesis and SAR of arylaminoethyl amides as noncovalent inhibitors of cathepsin S: P3 cyclic ethers, *Bioorg. Med. Chem. Lett.* 16 (2006) 5112–5117.
- [20] Cambridge Structural Database, 5.43 (2021).
- [21] W Lai, SM Berry, WP Kaplan, MS Hain, JC Poutsma, RJ Butcher, RD Pike, DC Bebout. Carbonate-templated self-assembly of an alkylthiolate-bridged cadmium macrocycle, *Inorg. Chem.* 52 (2013) 2286–2288.
- [22] HM Brennan, SG Bunde, Q Kuang, TV Palomino, JS Sacks, SM Berry, RJ Butcher, JC Poutsma, RD Pike, DC Bebout. Homo- and Heteronuclear Group 12 Metallothionein Type B Cluster Analogs: Synthesis, Structure, ^1H NMR and ESI-MS, *Inorg. Chem.* 61 (2022) 19857–19869.

- [23] JA Viehweg, SM Stamps, JJ Dertinger, RL Green, KE Harris, RJ Butcher, EJ Andriole, JC Poutsma, SM Berry, DC Bebout. A synthetic model of Hg(II) sequestration, Dalton Trans. 39 (2010) 3174–3176.
- [24] MR Hallinger, AC Gerhard, MD Ritz, JS Sacks, JC Poutsma, RD Pike, L Wojtas, DC Bebout. Metal substitution and solvomorphism in alkylthiolate-bridged Zn₃ and HgZn₂ Metal Clusters, ACS omega 2 (2017) 6391–6404.
- [25] S Itoh, M Nagagawa, S Fukuzumi. Fine Tuning of the Interaction between the Copper(I) and Disulfide Bond. Formation of a Bis(μ -thiolato)dicopper(II) Complex by Reductive Cleavage of the Disulfide Bond with Copper(I), J. Am. Chem. Soc. 123 (2001) 4087–4088.
- [26] H Kurosaki, T Tawada, S Kawasoe, Y Ohashi, M Goto. A model for ZnII-containing- β -lactamase: synthesis, X-ray crystal structure of a zinc(II) complex bearing thiol group and hydrolysis of phosphate diester, Bioorg. Med. Chem. Lett. 10 (2000) 1333–1337.
- [27] H Kurosaki, T Tawada, S Kawasoe, Y Ohashi, M Goto. Crystal Structure of Chloro{*N*-mercaptoethyl[bis(6-methyl-2-pyridylmethyl)amine]}zinc(II) complex, Anal. Sci.: X-Ray Struct. Anal. Online 19 (2003) x27–x28.

Chapter 3. Synthesis and characterization of bis-tridentate group 12 perchlorate complexes of bis(2-pyridylmethyl) ether

1. Introduction

Ether-containing bioactive compounds, including flavonoids, ionophores, carbohydrates, and a wide variety of pharmaceuticals, have metal-dependent bioactivity. Some flavonoids have been shown to have roles in zinc homeostasis [1,2] and ^1H NMR studies suggest that morin has a 1-ethero-2'-hydroxyl zinc binding site [3]. Ionophore complexes, specifically polyether ionophores, with group 12 metal centers have been shown to be effective antibacterial agents. They also show potential as anti-parasitic and anti-cancer agents [4–6]. A zinc azacrown ether complex has shown promise for biomedical applications [7]. The glucocorticoid budesonide helps treat the effects of cadmium exposure [8]. Flavonoids chelate with cadmium, preventing its accumulation [9]. These recent studies have motivated a comparative investigation of divalent group 12 metal ion coordination to a common ether ligand to obtain further potentially biologically relevant structural information.

Divalent group 12 metal ions are prone to rapid intermolecular ligand exchange and intramolecular reorganization because d^{10} metal ions are tolerant of a variety of coordination numbers and coordination geometries. To moderate the complexity of solution equilibria, multidentate ligand bis(2-pyridylmethyl) ether (**L2**, Fig. 1) was chosen for this study. Additional advantages of **L2** include ease of synthesis and previous group 12 coordination studies with related ligands **L3–L5**

[10–14]. In addition, several copper complexes of **L2** are known [15,16], including one with tyrosinase-like activity [17]. The meridional octahedral complex $[\text{Cr}(\text{L2})\text{Cl}_3]$ is a moderately active ethylene polymerization catalyst [18]. Meridional octahedral complexes $[\text{Fe}(\text{L2})\text{Cl}_3]$ and $[\text{Co}(\text{L2})_2](\text{PF}_6)$ have been examined for possible uses as reaction centers in oxidation and polymerization reactions [19]. Facial octahedral halide complexes $[\text{Rh}(\text{L2})\text{Cl}_3]$ [20] and $[\text{Mo}(\text{L2})(\text{CO})_3]$ [21] have been reported, as well as square pyramidal $[\text{Co}(\text{L2})\text{Cl}_2]$ [19]. The coordinative versatility of **L2** has been further demonstrated with trigonal bipyramidal $[\text{Zn}(\text{L2})\text{Cl}_2]$ and $[\text{Cd}(\text{L2})\text{Cl}_2]$ [22,23], as well as square pyramidal $[\text{Hg}(\text{L2})\text{Cl}_2]$ [24]. Significantly, several metal complexes of **L3–L5** with more than one equivalent of ligand are reported in the Cambridge Crystallographic Database [25], but only a single **L2** complex with more than one equivalent of ligand [24].

In this chapter, I report the synthesis of $[\text{Zn}(\text{L2})_2](\text{ClO}_4)_2 \cdot \text{CH}_3\text{CN}$ (**4**·CH₃CN), $[\text{Cd}(\text{L2})_2](\text{ClO}_4)_2 \cdot \text{CH}_3\text{CN}$ (**5**·CH₃CN) and $[\text{Hg}(\text{L2})_2](\text{ClO}_4)_2$ (**6**). The bis-tridentate chelate complexes are characterized by X-ray crystallography, ¹H NMR, IR spectroscopy, and TGA. The complexes are also compared to similar complexes of **L3**, **L4**, and **L5** (Fig. 1).

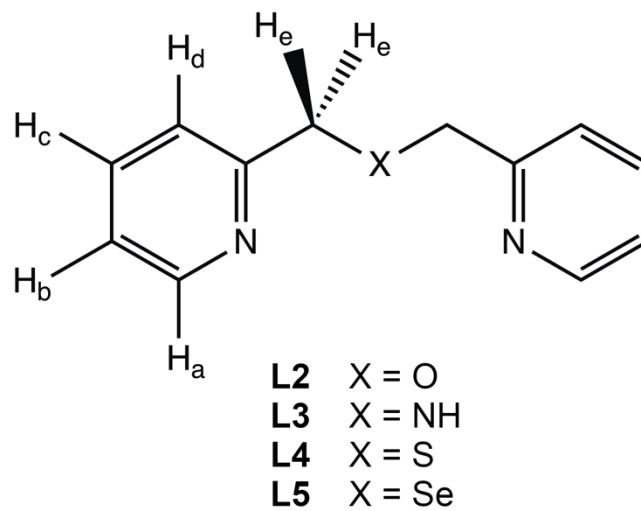


Figure 1. Structurally related N,X,N ligands.

2. Experimental

2.1 Reagents and Methods

Solvents and reagents were of commercial grade and used as received. Elemental analyses were carried out by Atlantic Microlab, Inc., Norcross, Georgia. ^1H NMR spectra were collected in 5 mm o.d. NMR tubes on an Agilent 400MR DD2 NMR spectrometer. IR spectra were collected on a Digital Labs FTS 7000 using a diamond ATR probe. Thermogravimetric analyses were collected on a Thermo Q500 with a ~4 mg sample heated in a flow of nitrogen from 25 °C to 800 °C.

X-ray diffraction data were collected on a Bruker SMART Apex DUO three-circle diffractometer system with a graphite monochromator, CCD detector using φ and ω scans, and Cu $K\alpha$ microfocus sealed tube ($\lambda = 1.54178 \text{ \AA}$) for **4**·CH₃CN and Mo $K\alpha$ fine-focus sealed tube ($\lambda = 0.71073 \text{ \AA}$) for **5**·CH₃CN and **6**. Selected crystallographic data are given in Tables 1 and 2. The structures were solved by direct methods or intrinsic phasing and refined on F^2 by full-matrix least squares using the ShelXle [26] program package. All non-hydrogen atoms were refined anisotropically and the hydrogens were placed theoretically.

CAUTION! Perchlorate salts of metal complexes with organic ligands are potentially explosive and should be handled with great care. Only small amounts of these materials were prepared [27,28]

Table 1. Crystallographic data for [Zn(L2)₂](ClO₄)₂·CH₃CN (**4**·CH₃CN), [Cd(L2)₂](ClO₄)₂·CH₃CN (**4**·CH₃CN), and [Hg(L2)₂](ClO₄)₂ (**6**)

	4 ·CH ₃ CN	5 ·CH ₃ CN	6
Empirical Formula	C ₂₆ H ₂₇ Cl ₂ N ₅ O ₁₀ Zn	C ₂₆ H ₂₇ CdCl ₂ N ₅ O ₁₀	C ₂₄ H ₂₄ Cl ₂ HgN ₄ O ₁₀
Formula mass [g mol ⁻¹]	705.79	752.82	799.96
Crystal Size [mm]	0.238 x 0.195 x 0.001	0.197 x 0.097 x 0.061	0.424 x 0.397 x 0.260
Crystal System	Monoclinic	Monoclinic	Monoclinic
Space Group	<i>P</i> 2 ₁	<i>P</i> 2 ₁	<i>P</i> 2 ₁ / <i>c</i>
<i>a</i> [Å]	8.5793(2)	8.529(14)	11.8815(5)
<i>b</i> [Å]	19.7007(3)	19.96(3)	14.6760(7)
<i>c</i> [Å]	8.6539(2)	8.910(14)	15.5350(7)
β[°]	91.6730(10)	93.87(2)	94.6680(10)
<i>V</i> [Å ³]	1462.04(5)	1513(4)	2699.9(2)
<i>Z</i>	2	2	4
Radiation (monochromatic)	Cu <i>K</i> α	Mo <i>K</i> α	Mo <i>K</i> α
<i>T</i> [K]	100(2)	100(2)	100(2)
ρ _{calc} [g cm ⁻³]	1.603	1.652	1.968
λ [Å]	1.54178	0.71073	0.71073
μ [mm ⁻¹]	3.424	0.962	5.963
Measured reflections	27189	23125	41476
Ind. reflections [<i>R</i> _(int)]	5081 (0.0646)	5927 (0.0323)	5474 (0.0201)
Completeness to [θ]	97.9%	100.0 %	100.0 %
Data / restraints / parameters	5081 / 353 / 393	5927 / 1 / 398	5474 / 0 / 370
<i>R</i> 1 ^a , <i>wR</i> 2 ^b [<i>I</i> > 2σ(<i>I</i>)]	0.0575, 0.1571	0.0270, 0.0613	0.0160, 0.0375
<i>R</i> 1 ^a , <i>wR</i> 2 ^b (all data)	0.0593, 0.1582	0.0293, 0.0621	0.0169, 0.0378
Goodness-of-fit (GOF)	1.136	1.058	1.082
Flack parameter	0.04(4)	0.007(8)	—

^a *R*1 = $\sum ||F_o| - |F_c|| / \sum |F_o|$, and *S* = $[\sum (w(F_o^2 - F_c^2)^2) / (n - p)]^{1/2}$; ^b *wR*2 = $[\sum (w(F_o^2 - F_c^2)^2) / \sum (w(F_o^2)^2)]^{1/2}$

Table 2. Selected bond lengths (Å) and angles (°) for [Zn(**L2**)₂](ClO₄)₂·CH₃CN (**4**·CH₃CN), [Cd(**L2**)₂](ClO₄)₂·CH₃CN (**5**·CH₃CN) and [Hg(**L2**)₂](ClO₄)₂ (**6**)

	4 ·CH ₃ CN (M = Zn)	5 ·CH ₃ CN (M = Cd)	6 (M = Hg)
M–N1	2.116(7)	2.299(5)	2.364(2)
M–N2	2.122(7)	2.291(5)	2.2289(19)
M–N3	2.136(7)	2.296(5)	2.2401(19)
M–N4	2.132(7)	2.291(5)	2.3928(19)
M–O1	2.196(6)	2.375(5)	2.6208(16)
M–O2	2.169(6)	2.376(5)	2.6778(15)
N1–M–N2	144.8(3)	136.90(16)	113.72(7)
N1–M–N3	96.4(3)	103.00(16)	94.93(7)
N1–M–N4	92.7(3)	93.90(16)	98.67(7)
N1–M–O1	72.3(2)	68.64(13)	67.87(6)
N1–M–O2	110.7(3)	121.97(13)	148.20(6)
N2–M–N3	95.6(2)	93.67(16)	142.93(7)
N2–M–N4	95.9(3)	100.18(16)	87.34(7)
N2–M–O1	72.8(2)	68.75(13)	68.83(6)
N2–M–O2	104.4(3)	101.38(15)	93.75(6)
N3–M–N4	145.3(3)	137.33(16)	112.05(7)
N3–M–O1	103.8(2)	104.69(16)	103.95(6)
N3–M–O2	73.4(2)	69.07(14)	68.76(6)
N4–M–O1	110.8(3)	117.95(14)	142.63(6)
N4–M–O2	72.0(3)	68.69(13)	65.52(6)
O1–M–O2	176.0(2)	168.44(12)	141.06(5)
M–O1–C6	121.3(5)	120.6(3)	108.18(13)
M–O1–C7	120.7(5)	120.9(3)	102.24(12)
M–O2–C18	121.9(5)	120.1(3)	104.26(12)
M–O2–C19	120.6(5)	119.8(3)	101.02(12)

2.2. Synthesis and characterizations

2.2.1. Synthesis of **L2**

L2 was synthesized by published procedures with minor changes [17]. ^1H NMR (CD_3CN , 20 °C) δ : 8.53 (d, 2H, $J = 4.8$ Hz, H_A), 7.77 (ddd, 2H, $J = 7.8, 7.8, 1.9$ Hz, H_C), 7.51 (d, 2H, $J = 7.7$ Hz, H_D), 7.26 (dd, 2H, $J = 7.7, 5.0$ Hz, H_B), 4.71 (s, 4H, H_E).

2.2.2. Synthesis of $[\text{Zn}(\text{L2})_2](\text{ClO}_4)_2 \cdot \text{CH}_3\text{CN}$ (**4**· CH_3CN)

A solution of $\text{Zn}(\text{ClO}_4)_2 \cdot 6\text{H}_2\text{O}$ (82 mg, 220 μmol) was added to two equivalents of **L2** (87 mg, 437 μmol) in 3 mL of acetonitrile. The resulting precipitate was dissolved by sonication after adding 3 mL of acetonitrile. Meta-xylene was added to reach the saturation point. The solution was filtered through Celite and fractionated. Colorless plates were obtained through slow evaporation (35 mg, 52 μmol , 24% yield). MP: 235 °C (dec.). ^1H NMR (CD_3CN , nominally 2 mM, 20 °C) δ : 8.15 (d, 2H, $J = 5.3$ Hz, H_a), 8.00 (ddd, 2H, $J = 8.2, 8.2, 1.8$ Hz, H_c), 7.60 (d, 2H, $J = 8.3$ Hz, H_d), 7.36 (dd, 2H, $J = 7.6, 5.1$ Hz H_b), 5.52 (s, 4H, H_e). IR (ATR) ν/cm^{-1} : 563.21 (w), 621.08 (s), 644 (w), 727 (m), 766 (s), 814 (w), 899 (w), 932 (w), 970 (w), 1022 (s), 1053 (w), 1072 (s), 1130 (w), 1132 (w), 1161 (w), 1292 (m), 1364 (w), 1404 (w), 1445 (m), 1470 (w), 1491 (w), 1612 (m). Elemental analysis calculated for $\text{C}_{24}\text{H}_{24}\text{Cl}_2\text{N}_4\text{O}_{10}\text{Zn} \cdot 0.7(\text{CH}_3\text{CN})$ (partial desolvation of **4**· CH_3CN assumed to occur during vacuum drying): C, 43.99; H, 3.80; N, 9.49. Found: C, 42.76; H, 3.83; N, 9.21.

2.2.3. Synthesis of $[\text{Cd}(\text{L2})_2](\text{ClO}_4)_2 \cdot \text{CH}_3\text{CN}$ (**5**·CH₃CN)

A solution of $\text{Cd}(\text{ClO}_4)_2 \cdot 6\text{H}_2\text{O}$ (55.8 mg, 133 μmol) in 2.25 mL of acetonitrile was added dropwise to three equivalents of **L2** (79.8 mg, 399 μmol) in 2.25 mL of acetonitrile. The solution was filtered through Celite. Colorless blocks formed through slow diffusion with ether (57.8 mg, 81.3 μmol , 61.1% yield). MP: 247 °C (dec.). ¹H NMR (CD_3CN , nominally 2 mM, −40 °C) δ : 8.21 (d, 2H, $J = 4.9$ Hz, H_a), 8.01 (ddd, 2H, $J = 7.8, 7.8, 1.4$ Hz, H_c), 7.56 (d, 2H, $J = 8$ Hz, H_d), 7.41 (dd, 2H, $J = 7.6, 5.2$ Hz, H_b), 5.32 (s, 4H, H_e). IR (ATR) ν/cm^{-1} : 621 (s), 644 (m), 727 (m), 766 (s), 810 (w), 897 (w), 1020 (s), 1072 (s), 1123 (w), 1163 (w), 1227 (w), 1294 (m), 1366 (m), 1406 (w), 1443 (m), 1466 (w), 1493 (m), 1574 (w), 1607 (s), 3593 (w). Elemental analysis calculated for $\text{C}_{24}\text{H}_{24}\text{Cl}_2\text{CdN}_4\text{O}_{10}$ (desolvation of **5**·CH₃CN assumed to occur during vacuum drying): C, 40.50; H, 3.40; N, 7.87. Found: C, 40.44; H, 3.48; N, 7.95.

2.2.4. Synthesis of $[\text{Hg}(\text{L2})_2](\text{ClO}_4)_2$ (**6**)

A solution of $\text{Hg}(\text{ClO}_4)_2 \cdot 3\text{H}_2\text{O}$ (94 mg, 208 μmol) in 2.25 mL of acetonitrile was added to two equivalents of **L2** (83 mg, 416 μmol) in 2.25 mL of acetonitrile. The solution was filtered through Celite. Colorless needles formed through slow diffusion with ether (38 mg, 48 μmol , 23% yield). MP: 152 °C (dec.). ¹H NMR (CD_3CN , nominally 2 mM, 20 °C) δ : 8.15 (d, 2H, $J = 5.2$ Hz, $J_{\text{HgH}} = 42.4$ Hz, H_a), 8.11 (ddd, 2H, $J = 8.4, 8.4, 1.5$ Hz, H_c), 7.71 (d, 2H, $J = 8$ Hz, $J_{\text{HgH}} = 22.8$ Hz, H_d), 7.53 (dd, 2H, $J = 7.8, 5.0$ Hz, H_b), 5.07 (s, 4H, H_e). IR (ATR) ν/cm^{-1} : 619 (s), 640 (w), 652 (m), 733 (w), 758 (s), 816 (w), 847 (w), 934 (m), 943 (w), 967 (w), 999 (w), 1016 (w), 1055 (m), 1070 (s), 1107 (w), 1163 (w), 1271 (w), 1308 (w), 1375

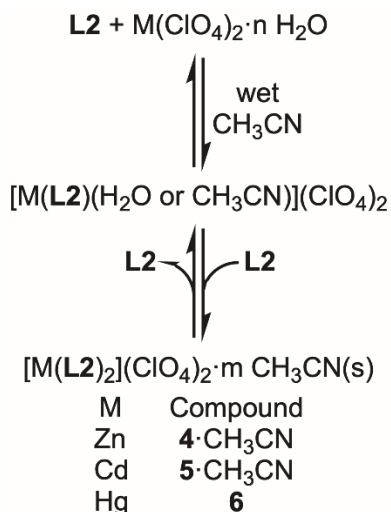
(w), 1439 (m), 1449 (w), 1487 (w), 1607 (m). Elemental analysis calculated for $C_{24}H_{24}Cl_2HgN_4O_{10}$: C, 36.03; H, 3.02; N, 7.00. Found: C, 35.87; H, 2.89; N, 6.99.

3. Result and Discussion

3.1. Syntheses

New compounds with $[M(\mathbf{L2})_2]^{2+}$ ($M = \text{Zn, Cd or Hg}$) complex ions were prepared by self-assembly in acetonitrile solutions containing at least two equivalents of **L2** per equivalent of vacuum dried metal perchlorate hydrate with $[M(\mathbf{L2})(\text{H}_2\text{O or CH}_3\text{CN})]^{2+}$ as a presumed intermediary species (Scheme I) [10]. Colorless plates of $[\text{Zn}(\mathbf{L2})_2](\text{ClO}_4)_2 \cdot \text{CH}_3\text{CN}$ (**4**·CH₃CN) were obtained in modest yield through slow evaporation with m-xylene as a cosolvent. The zinc(II) complex had satisfactory elemental analysis based on partial loss of acetonitrile during brief vacuum drying. The attempted synthesis of **5** by slow evaporation from acetonitrile solutions with 1:2 Cd(II):**L2** and meta-xylene as cosolvent produced a heteromorphic solid containing diffraction quality crystals of **5**·CH₃CN. Characterization of the solid in CD₃CN by proton NMR revealed two sets of broadened ligand peaks. Elemental analyses of vacuum dried solids suggested co-isolation of **5** and variable amounts of $[\text{Cd}(\mathbf{L2})(\text{H}_2\text{O})](\text{ClO}_4)_2$. When grown from an acetonitrile solution with 1:3 Cd(II):**L2** ratio by slow diffusion with ether, crystals of **5**·CH₃CN were obtained in high yield without significant contamination from $[\text{Cd}(\mathbf{L2})(\text{H}_2\text{O})](\text{ClO}_4)_2$ based on both NMR and elemental analysis of the vacuum dried solid. Finally, colorless needles of $[\text{Hg}(\mathbf{L2})_2](\text{ClO}_4)_2$ (**6**) with satisfactory elemental analysis were obtained in modest yield through slow diffusion between acetonitrile solutions with 1:2 Hg(II):**L2** and ether. Complex **6** had distinctive $J(^{199}\text{Hg}^1\text{H})$ coupling satellites around the four pyridyl proton resonances in CD₃CN at $-40\text{ }^\circ\text{C}$ (*vide infra*). Satellites were broadened (H_a, H_d) or lost (H_b, H_c) at room

temperature consistent with onset of an exchange process such as full or partial ligand dissociation. We did not explore whether decreasing the metal:ligand ratio improved the yield of **4**·CH₃CN or **6**. Limited attempts to crystallize 1:1 complexes of M(ClO₄)₂ (M = Zn, Cd, and Hg) and **L2** were unsuccessful.



Scheme 1. Proposed self-assembly process for complexes of **L2**

3.2. Structures of $[\text{Zn}(\text{L2})_2](\text{ClO}_4)_2 \cdot \text{CH}_3\text{CN}$ (**4**·CH₃CN) and $[\text{Cd}(\text{L2})_2](\text{ClO}_4)_2 \cdot \text{CH}_3\text{CN}$ (**5**·CH₃CN)

Isomorphous **4**·CH₃CN and **5**·CH₃CN crystallized in monoclinic space group *P*2₁. In addition to one complex ion and two perchlorate ions, the asymmetric units contain an acetonitrile molecule of solvation. The perchlorate oxygens and solvent molecules are well separated from the metal ions. Selected bond distance and angles for the complex ions of **4** and **5** are shown in Table 2.

Complex ion **4** has a nearly ideal meridional octahedral structure as shown in Figure 2. The heavy atoms of each ligand are nearly coplanar. The dihedral

angles between the mean square Zn–N–C–C–O planes sharing an oxygen atom are under 6° . The angle between the N1–O1–N2 and N3–O3–N4 planes is 88.33° . The O1–Zn–O2 angle was $176.0(2)^\circ$, approaching the ideal value of 180° . Chelate ring constraints give rise to much smaller average trans N–Zn–N angles ($145.1(4)^\circ$). Notably, the Zn–O bond lengths range $2.169(6)$ – $2.196(6)$ Å, approaching the minimum observed for structurally characterized Zn(II) complexes with $\text{N}_4\text{O}(\text{ether})_2$ coordination spheres (2.169 – 2.692 Å) [25]. Furthermore, the highly flattened ligand geometry, small N–Zn–O–C torsion angles (1.6 – 9.8°), and small oxygen thermal ellipsoids suggest sp^2 hybridization of the ether oxygen. Similar ether oxygen geometries have been observed for a wide range of structurally characterized metal complexes [25].

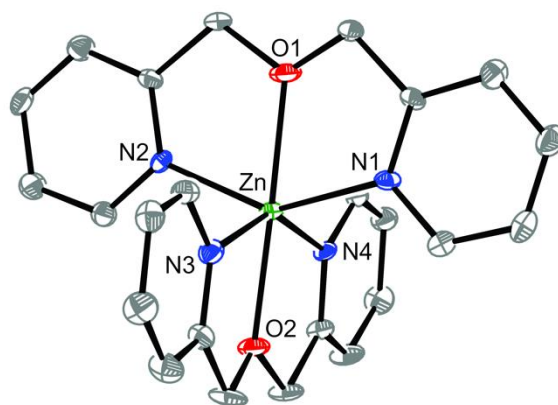


Figure 2. Thermal ellipsoid (50% probability) structure for the complex ion of **5**·CH₃CN. Hydrogen atoms, perchlorate anions, and CH₃CN solvent molecule are omitted for clarity

The pseudo- C_{2v} complex symmetry is favorable for extensive supramolecular interactions between pyridyl rings [29]. Attractive aromatic interactions observed between the complex ions include a concerted orthogonal fourfold aryl embrace involving four pyridyl rings from neighboring molecules with centroid distances ranging from 4.890–5.166 Å (Fig. 3). These are networked into extended sheets by additional intermolecular offset face-to-face π – π (OFF) interactions between the N1 and N2 pyridyl rings and the N3 and N4 pyridyl rings with centroid distances of 3.660 Å and 3.659 Å, respectively. These supramolecular interactions likely contribute to the highly planar ligand conformations.

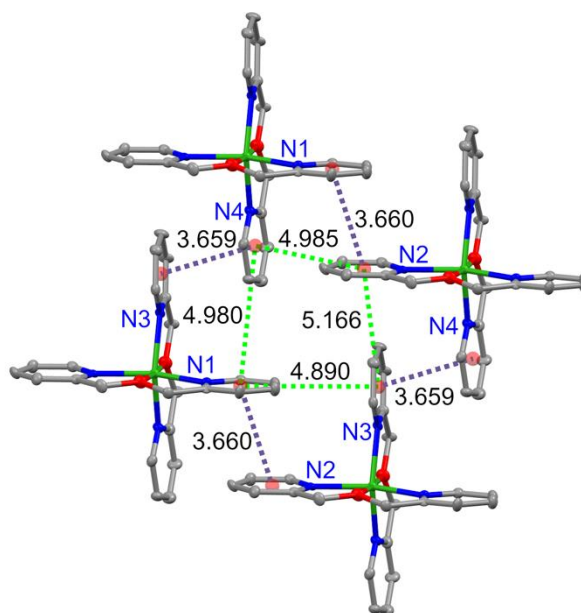


Figure 3. Intermolecular aromatic stacking interactions of the pyridyl rings, identified by their nitrogen atoms, in **4**·CH₃CN. Hydrogen atoms, perchlorate ions and solvent molecules are omitted for clarity. The OFF interactions are colored purple and the EF interactions are green

The complex ion **5**·CH₃CN has a more distorted meridional octahedral geometry (Fig. 4). The heavy atoms of each ligand are nearly coplanar, though less so than in **4**. The dihedral angles between the mean square Cd–N–C–C–O planes sharing an oxygen atom are between 6–8°. The ligands are also almost perpendicular to each other, with an angle of 82.95° between the N1–O1–N2 and N3–O2–N4 planes. The O1–Cd–O2 angle and the trans N–Cd–N angles are further from ideal than their counterparts in the Zn complex. The bond length ranges for Cd–N (2.291–2.299 Å) and Cd–O (2.375–2.376 Å) are very small, with a larger difference between them than the related bonds in **4**. Notably, the Cd–O bond lengths approach the minimum observed for structurally characterized Cd(II) complexes with N₄O(ether)₂ coordination spheres (2.374–2.797 Å). In addition, **5** has flattened ligand geometry, small N–Cd–O–C torsion angles (5.6–15.4°), and small oxygen thermal ellipsoids similar to **4**.

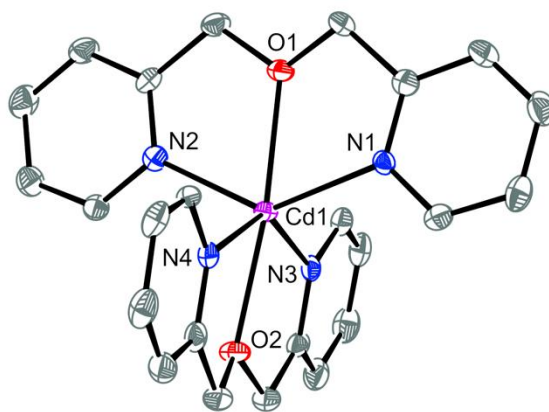


Figure 4. Thermal ellipsoid (50% probability) structure for the complex ion of **5**·CH₃CN. Hydrogen atoms, perchlorate counterions, and the CH₃CN solvent molecule are omitted for clarity.

Supramolecular constraints in **5** are relaxed relative to **4**. The fourfold aryl embrace ring centroid distances range from 4.997–5.686 Å (Fig. 5). Increased spacing between complex ions and greater distortion from meridional octahedral geometry are congruous. The OFF interactions in **5** had centroid distances between the N1 and N2 pyridyl rings and the N3 and N4 pyridyl rings of 3.696 and 3.650 Å, respectively, quite comparable to **4**.

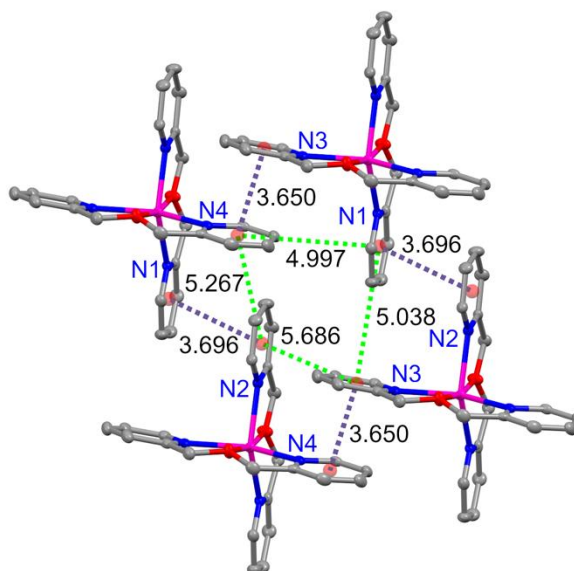


Figure 5. Intermolecular aromatic stacking interactions of the pyridyl rings, identified by their nitrogen atoms, in **5**·CH₃CN. Hydrogen atoms, perchlorate ions and solvent molecule are omitted for clarity. The OFF interactions are colored purple, and the EF interactions are green.

Square pyramidal complexes [Zn(**L2**)Cl₂] ($\tau = 0.03$) and [Cd(**L2**)Cl₂] ($\tau = 0.11$) have somewhat less planar ligand conformations with mean square chelate

ring torsion angles between 8.60–10.43° [22,23]. The other structurally characterized bis-tridentate chelates of Zn and Cd involving an N,O,N ligand have similar meridional octahedral complex ion structures, however they show a wider range of chelate ring torsion angles. The less distorted octahedral complexes have angles ranging from 0.29–8.75° [30–32] while some Cd complexes are more distorted with torsion angles ranging from 20.57–23.84 [33,34]. Bis-tridentate chelates of Zn and Cd with related ligands **L3**, **L4**, and **L5** (Fig. 1) are known, however, none of these complexes had meridional octahedral solid-state structures (Table 3).

Table 3. Selected bond lengths (Å) and angles (°) for complex ions of [M(L)₂](ClO₄)₂ (L = **L2–L5**)

L	M	Δ (Å) ^a	X–M–X	N–M–N	Coord. Geo. ^b	Reference
L2 X = O	Zn (4)	0.056	176.0(2)	144.8(3), 143.3(3)	15	This work
	Cd (5)	0.081	168.44(12)	136.90(16), 137.33(16)	15	"
	Hg (6)	0.3429	141.06(5)	113.72(7), 112.05(7)	14, 14'	"
L3 X = N	Zn	0.003	130.5(3)	117.4(2)	14, 14'	[10]
	Zn	0.159	180	180	12, 12'	"
	Cd	0.033	142.2(2)	114.7(2), 112.5(2)	14, 14'	[12]
	Hg	−0.058	153.1(2)	108.5(2), 116.4(2)	14, 14'	[11]
L4 X = S	Zn	0.3105	180.00	82.38(5)	10	[13]
	Cd	0.332	126.264(19)	112.66(7), 112.71(7)	12, 12'	"
	Hg	0.212	143.23(3)	74.61(12), 77.19(12)	11, 11'	"
	Hg	0.164	141.04(4)	76.52(13), 75.98(12)	11, 11'	"
L5 X = Se	Cd	0.401	167.788(16)	97.37(11), 77.71(11)	10	[14]
	Hg	−0.003	135.98(3)	72.3(2), 72.36(19)	11, 11'	"

^a Δ = Average M–X – Average M–N_{pyridyl}

^b See Fig. 6

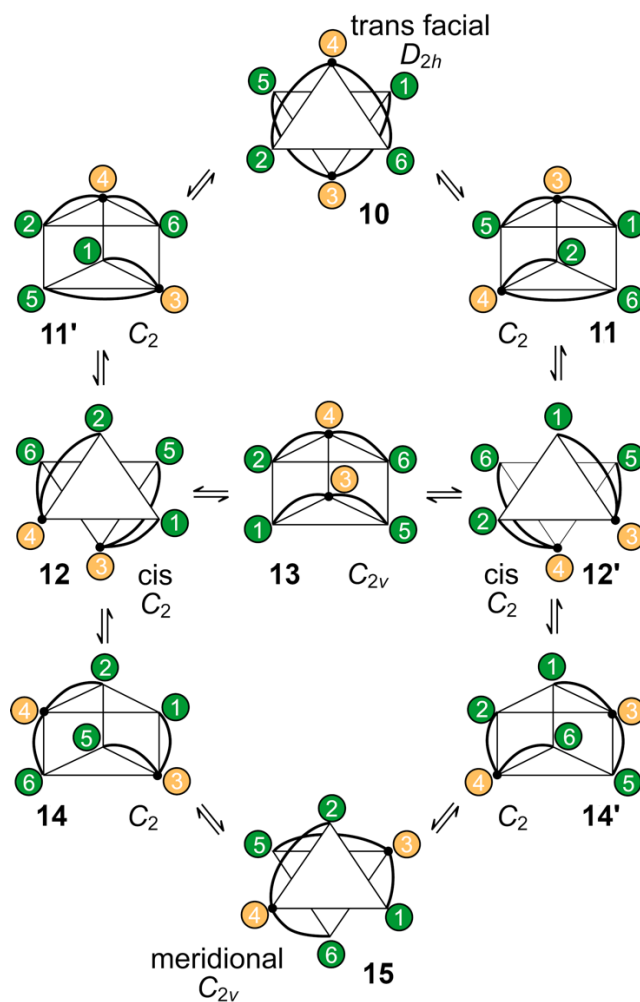


Figure 6. The nine isomeric forms of bis-tridentate chelates.

3.3. Structure of $[Hg(L2)_2](ClO_4)_2$ (**6**)

Complex **6** crystallized in the monoclinic space group $P2_1/c$ as an enantiomeric pair of complexes with distorted trigonal prismatic coordination geometry (Fig. 7). One triangular face consists of atoms O1, N1, and N3, which individually almost eclipse N2, N4, and O2, respectively. A rectangular face is capped by O8 of one perchlorate ion. The Hg–O8 distance of 3.161 Å is within the

sum of van der Waals radii ($\text{Hg} = 1.75\text{\AA}$ [35], $\text{O} = 1.52\text{\AA}$ [36]). A pseudo- C_2 axis lies roughly along the $\text{Hg}-\text{O8}$ bond.

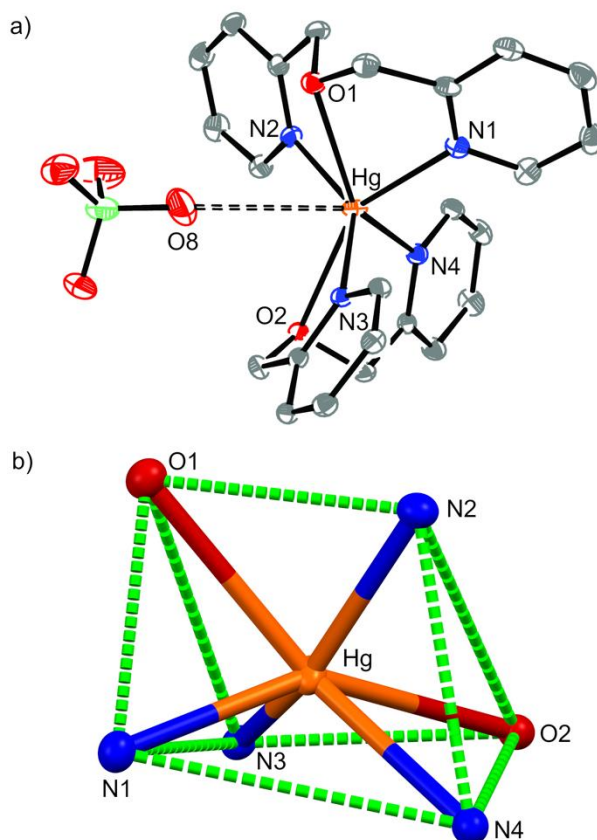


Figure 7. (a) Thermal ellipsoid (50% probability) structure of the $[\text{Hg}(\mathbf{L2})_2](\text{ClO}_4)^+$ ion pair of **6**. Hydrogen atoms are omitted for clarity. (b) Overview of trigonal prismatic $\text{Hg}(\text{II})$ coordination environment.

The $\text{Hg}-\text{O}$ bond distances involving **L2** are similar to each other. The five-membered chelate rings are in an envelope conformation, with the oxygen at the apex in a tripodal geometry suggesting sp^3 hybridization. The $\text{N}-\text{Hg}-\text{O}-\text{C}$ torsion angles range from 25.1 – 40.0° , much larger than their counterparts in **4**· CH_3CN and **5**· CH_3CN . The displacement of O1 from the mean square N1 and N2 chelate

ring planes is 0.574 Å and 0.661 Å, respectively. The N2 and N4 chelate rings are more puckered with O2 displaced 0.800 Å and 0.920 Å, respectively. Unlike complexes **4**·CH₃CN and **5**·CH₃CN, no π – π interactions were observed in the crystal structure. The distorted trigonal prismatic solid-state structure is comparable to pnictogen-donor exclusive complex [Hg(**L3**)₂](ClO₄)₂ but different than chalcogen-donor inclusive complexes [Hg(**L4**)₂](ClO₄)₂ and [Hg(**L5**)₂](ClO₄)₂ (Table 3).

There are a variety of structurally characterized complexes with tridentate N,O,N ligands bound to Hg(II) [25], however, square pyramidal [Hg(**L2**)Cl₂] (τ = 0.07) is the only documented complex with an ether bound to the metal center [24]. The ligand in [Hg(**L2**)Cl₂] has a more planar conformation than either **L2** in **6**. The dihedral angle between the mean square N–C–C–O planes is 16.47°. The dihedral angles between the corresponding planes in **6** are significantly larger: 69.06° for the planes sharing O1 and 72.59° for the planes sharing O2. However, the N–Hg–O–C torsion angles of 29.59° and 37.19°, within the range of the corresponding torsion angles of **6**. The only other structurally characterized Hg(II) complexes with N₄O(ether)₂ coordination spheres are based on ethoxyphenyltriazenes and have highly distorted meridional octahedral coordination geometries [37-39]. There are few examples in the literature of N_xO_y ligands with both an ether connected to the metal center and an sp² nitrogen. Seven and eight-coordinate Hg(II) complexes have been made from the five-coordinate ligand 2,6-bis[[(2-pyridinylmethyl)oxy)methyl]pyridine [40,41]. The ligand (2-methyl-8-(6-(diethylaminoacetate)methylene-pyridin-2-ylmethoxy)quinoline) can form 4- and 5-

coordinate complexes with Hg(II), in which the heteroatoms of the ligand are planar to each other. These examples show Hg–O bonds ranging from 2.51–2.764 Å, which encompasses the length range for Hg–O bonds in **6**; the literature range of Hg–N bond lengths is 2.066–2.81 Å, much larger than the range observed in **6** [37–42].

3.4. Solution State NMR characterization

Variable temperature ^1H NMR was used to study complexes **4**, **5**, and **6** in CD_3CN solution (Fig. 8). While correlations between solid-state and solution-state spectroscopy are rarely definitive for group 12 metal ion complexes due to intramolecular reorganization, intermolecular exchange and variable oligomerization, at both $-40\text{ }^\circ\text{C}$ and $20\text{ }^\circ\text{C}$ each of the complexes had a single set of four pyridyl proton resonances and a singlet methylene proton resonance, reflecting relaxation of solid-state constraints as well as a process making the methylene protons of **6** equivalent. With the exception of H_a , all resonances were shifted downfield of the free ligand as expected due to the deshielding influence of σ donation to a metal ion. The upfield shift of H_a is likely associated with exposure to the ring current of the opposite ligand (Fig. 9). While H_a is not well positioned for ring current exposure in the meridional octahedral geometry in which **4** and **5** were isolated, bis-tridentate chelates are known to undergo facile isomerization between many of the nine isomeric forms by rotations about pseudo- C_3 axes of the pseudo-octahedral and pseudo-trigonal prismatic ligating atom cores (Fig. 6). The ^1H NMR spectra of complexes **4** and **5** are very similar to each other in the aromatic region, consistent with similar overall isomer distribution in solution.

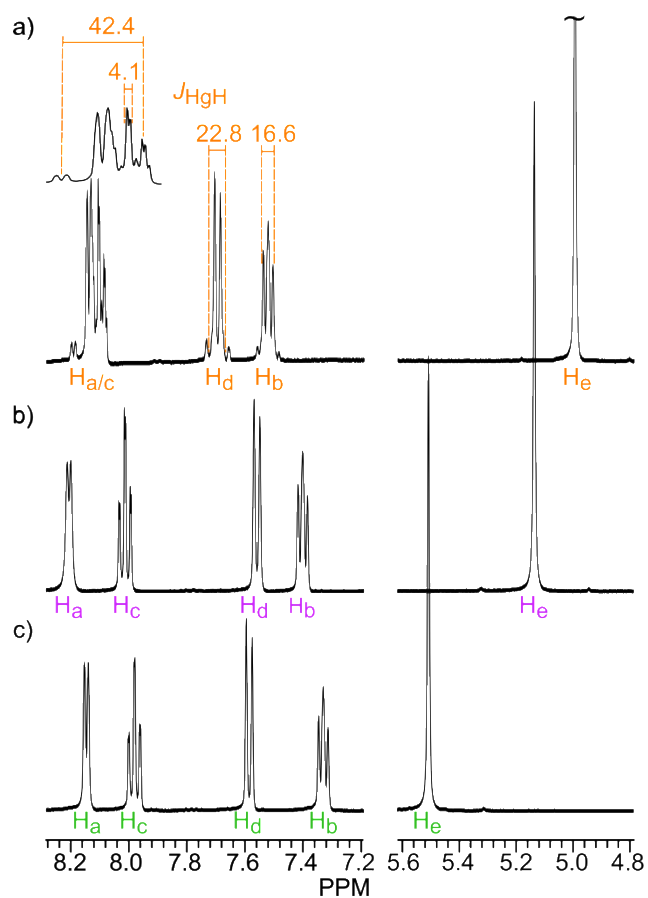


Figure 8. ^1H NMR (CD_3CN , nominally 2 mM, $-40\text{ }^\circ\text{C}$) for a) $[\text{Hg}(\text{L}2)_2](\text{ClO}_4)_2$ (6) b) $[\text{Cd}(\text{L}2)_2](\text{ClO}_4)_2 \cdot \text{CH}_3\text{CN}$ (5· CH_3CN) and c) $[\text{Zn}(\text{L}2)_2](\text{ClO}_4)_2 \cdot \text{CH}_3\text{CN}$ (4· CH_3CN).

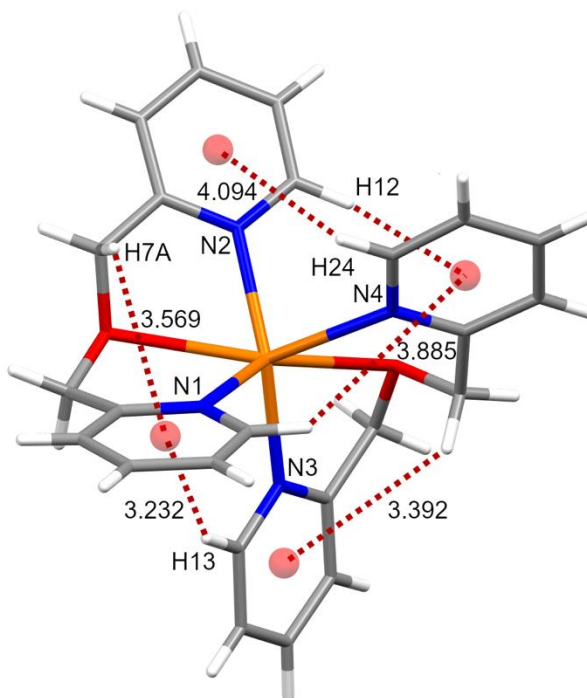


Figure 9. Ring current interactions between pyridyl rings and hydrogens on pyridyl rings of the opposing ligand in the complex ion of **6**.

Significantly, **6** exhibits prominent heteronuclear $J(^{199}\text{Hg}^1\text{H})$ coupling to all the pyridyl ring protons at $-40\text{ }^{\circ}\text{C}$, confirming that the pyridyl nitrogen atoms remain bound to the metal ion on the coupling constant time scale. Heteronuclear coupling between H_e and ^{199}Hg was not resolved, consistent with either a very small coupling constant or cleavage of the $\text{Hg}-\text{O}$ bond on the coupling constant time scale. As the temperature is raised to $20\text{ }^{\circ}\text{C}$, the ligand chemical shifts of **6** move upfield modestly with loss of heteronuclear coupling to protons other than H_a consistent with onset of an exchange process that is rapid compared to the time scale of the smaller coupling constants as discussed in Section 3.1. Among related ligands, both **L3** and **L4** exhibited heteronuclear coupling with ^{199}Hg in the bis-

tridentate chelate (Table 4) [11]. Heteronuclear $J(^{111/113}\text{Cd}^1\text{H})$ coupling was not observed for **5** and has only been reported for **L3** in the analogous series of complexes highlighted (Table 4). Either smaller $J(^{111/113}\text{Cd}^1\text{H})$ coupling constants [13] or higher intermolecular ligand exchange rates may explain the absence of heteronuclear coupling in **5**. Heteronuclear coupling with the metal ion is not expected for **4** because zinc does not have a high natural abundance NMR active nuclide.

Table 4. Observed heteronuclear coupling constants (Hz) for $[\text{M}(\text{L})_2]^{2+} (\text{CD}_3\text{CN})^a$

Ligand	L2^b	L3^b		L4^c
Metal	Hg (3)	Cd	Hg	Hg
H _a	42.4	6	20	24
H _b	16.6	–	–	8
H _c	4.1	–	–	8
H _d	22.8	–	–	10
H _e	–	–	72, 69	56
Reference	This work	[17]	[16]	[18]

^a Proton NMR are not available for complexes of **L5**; ^b –40 °C; ^c –20 °C.

At both –40 and 20°C, a singlet is observed for the methylene protons (H_e) of compounds **4–6**. A singlet for the methylene is expected for **4** and **5** as their solid-state structures have nearly C_{2v} symmetry. In contrast, the methylene protons of pseudo- C_2 **6** would be expected to have two environments after the relaxation

of solid-state constraints if intramolecular reorganization between isomeric forms was slow but were detected as a singlet. Similarly, $[\text{Hg}(\text{L4})_2]^{2+}$ had a singlet methylene resonance at readily accessible temperatures [13,14]. In contrast, under cryogenic conditions the methylene protons of $[\text{Hg}(\text{L3})_2]^{2+}$ gave rise to a geminally coupled doublet of doublets, suggesting that the meridional octahedral geometry does not contribute significantly to solution equilibria. A significantly lower barrier for inversion of chalcogens likely enhances the methylene proton exchange rate. Interestingly, the methylene singlet shifts upfield significantly down group 12. In bis-tridentate chelates of ligands **L3** and **L4**, this trend is absent [11-14].

3.5. Thermogravimetric Analysis

Thermogravimetric analysis was used to determine the thermal stability of **4**·CH₃CN, **5**·CH₃CN, and **6** (Fig. 10). Complex **4**·CH₃CN shows its first weight loss (Obsd. 5.5%, Calcd. 5.8%) from 40 °C to 116 °C, corresponding to acetonitrile. The second weight loss (Obsd 84.8%, Calcd. 84.9%) at 326 °C shows vigorous decomposition of the ligand and perchlorates, leaving only the Zn metal (Obsd 9.7%, Calcd. 9.3%) and suggesting the complex resists thermal decomposition up to the point where perchlorate becomes unstable. Complex **5**·CH₃CN exhibits a three-step decomposition. Loss of residual acetonitrile occurs below 243°C (Obsd 2.4%, Calcd. 5.5%) followed by multi-stage ligand loss from 280 °C to 541 °C (Obsd. 53.0%, Calcd. 53.2%). Gradual loss of cadmium perchlorate is nearing completion at 780 °C (Obsd. 42.3%, Calcd. 43.7%). The decomposition of complex **6** is a multi-stage process, happening from 191 °C to 501 °C, with Hg remaining

(Obsd. 74.4%, Calcd. 74.9%). Following solvent loss, decomposition temperatures increase with metal hardness, qualitatively consistent with predictive hard and soft acid and base trends.

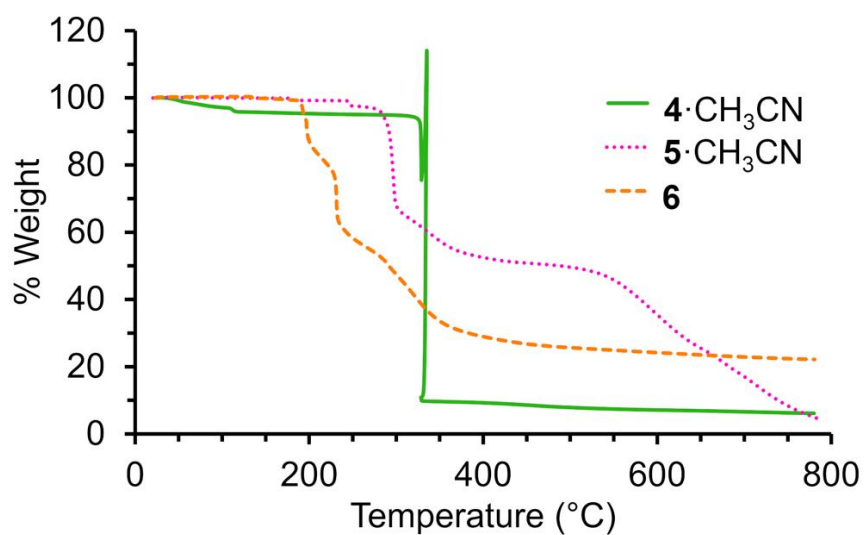


Figure 10. TGA curves for 4·CH₃CN, 5·CH₃CN, and 6.

4. Conclusion

Bis-tridentate complexes of $\text{Zn}(\text{ClO}_4)_2$, $\text{Cd}(\text{ClO}_4)_2$, and $\text{Hg}(\text{ClO}_4)_2$ with the ligand bis(2-pyridylmethyl) ether (**L2**) were isolated. $[\text{Zn}(\text{L2})_2](\text{ClO}_4)_2 \cdot \text{CH}_3\text{CN}$ and $[\text{Cd}(\text{L2})_2](\text{ClO}_4)_2 \cdot \text{CH}_3\text{CN}$ crystallized in the monoclinic space group $P2_1$ with meridional octahedral geometry. $[\text{Hg}(\text{L2})_2](\text{ClO}_4)_2$ crystallized in the space group $P2_1/c$ with a trigonal prismatic geometry. In addition to crystallographic characterization, these complexes were characterized using IR, ^1H NMR, and TGA. These complexes were then compared to related Group 12 complexes of similar ligands with different central heteroatoms. Complexes **4**· CH_3CN and **5**· CH_3CN provide the first structurally characterized meridional octahedral coordination geometry for bis-pyridyl N,X,N ligand complexes of group 12 metal ions. Complex **6** has the trigonal prismatic **14,14'** form in common with $[\text{Hg}(\text{L2})_2](\text{ClO}_4)_2$, differing from the trigonal prismatic **11,11'** form observed for other bis-tridentate chelates of Hg(II) with bis-pyridyl N,chalcogen,N ligands. The methylene protons of **L2** were equivalent in **6** by ^1H NMR at -40°C as found previously for the related thioether ligand, but not the amine ligand. This suggests that coordinated central chalcogens have a lower barrier to inversion when bound to Hg(II) compared to nitrogen.

References

- [1] K Sreenivasulu, P Raghu, KM Nair. Polyphenol-Rich Beverages Enhance Zinc Uptake and Metallothionein Expression in Caco-2 Cells, *J. Food Sci.* 75 (2010) H123–H128.
- [2] E Kim, T Pai, O Han. Effect of Bioactive Dietary Polyphenols on Zinc Transport across the Intestinal Caco-2 Cell Monolayers, *J. Agric. Food Chem.* 59 (2011) 3606–3612.
- [3] Y Wei, M Guo. Zinc-Binding Sites on Selected Flavonoids, *Biol. Trace Elem. Res.* 161 (2014) 223–230.
- [4] J Ivanova, IN Pantcheva, M Mitewa, S Simova, M Tanabe, K Osakada. Cd(II) and Pb(II) complexes of the polyether ionophorous antibiotic salinomycin, *Chem. Cent. J.* 5 (2011) 52–52.
- [5] M Antoszczak, D Steverding, A Huczynski. Anti-parasitic activity of polyether ionophores, *Eur. J. Med. Chem.* 166 (2019) 32–47.
- [6] A Huczynski. Polyether ionophores-promising bioactive molecules for cancer therapy, *Bioorg. Med. Chem. Lett.* 22 (2012) 7002–7010.
- [7] GY Aleshin, BV Egorova, AB Priselkova, LS Zamurueva, SY Khabirova, AD Zubenko, VA Karnoukhova, OA Fedorova, SN Kalmykov. Zinc and copper complexes with azacrown ethers and their comparative stability in vitro and in vivo, *Dalton Trans.* 49 (2020) 6249–6258.
- [8] W Zhang, J Zhi, Y Cui, F Zhang, A Habyarimana, C Cambier, P Gustin. Potentiated interaction between ineffective doses of budesonide and formoterol to control the inhaled cadmium-induced up-regulation of metalloproteinases and acute pulmonary inflammation in rats, *PLoS One* 9 (2014) e109136.
- [9] X Li, X Jiang, J Sun, C Zhu, X Li, L Tian, L Liu, W Bai. Cytoprotective effects of dietary flavonoids against cadmium-induced toxicity, *Ann. N. Y. Acad. Sci.* 1398 (2017) 5–19.
- [10] J Glerup, PA Goodson, DJ Hodgson, K Michelsen, KM Nielsen, H Weihe. Synthesis and characterization of bis(2-pyridylmethyl)amine complexes of manganese(II), zinc(II), and cadmium(II), *Inorg. Chem.* 31 (1992) 4611–4616.
- [11] DC Bebout, AE DeLanoy, DE Ehmann, ME Kastner, DA Parrish, RJ Butcher. Characterization of Mercury(II) Complexes of Bis[(2-pyridyl)methyl]amine by X-ray Crystallography and NMR Spectroscopy, *Inorg. Chem.* 37 (1998) 2952–2959.

- [12] DC Bebout, SW Stokes, RJ Butcher. Comparison of Heteronuclear Coupling Constants for Isostructural Nitrogen Coordination Compounds of $^{111/113}\text{Cd}$ and ^{199}Hg , *Inorg. Chem.* 38 (1999) 1126-1133.
- [13] SM Berry, DC Bebout, RJ Butcher. Solid-State and Solution-State Coordination Chemistry of the Zinc Triad with the Mixed N,S Donor Ligand Bis(2-methylpyridyl) Sulfide, *Inorg. Chem.* 44 (2005) 27–39.
- [14] BY Winer, SM Berry, RD Pike, DC Bebout, Synthesis of bis(2-pyridylmethyl)selenide and solid-state structural characterization of bis-tridentate zinc triad perchlorate chelates, *Polyhedron* 48 (2012) 125–130.
- [15] JM Li. Dichlorido[2,2'-(oxydimethyl-ene)dipyridine]copper(II), *Acta Crystallogr. Sect. E Struct. Rep. Online* 64 (2008) m1467.
- [16] H Li, LM Xie, SG Zhang. Chlorido[2,2'-(oxydimethyl-ene)-dipyridine]copper(II) perchlorate-aqua-chlorido[2,2'-(oxydimethyl-ene)-dipyridine]copper(II) perchlorate (1/1), *Acta Crystallogr. Sect. E Struct. Rep. Online* 65 (2009) m933.
- [17] Y Cheng, H Chen, S Tsai, C Su, H Tsang, T Kuo, Y Tsai, F Liao, S Wang. Structure, Bonding, and Tyrosinase-Like Reactivity of Copper Complexes Coordinated by Mononucleating Tridentate N–O–N Type Ligands, *Eur. J. Inorg. Chem.* 2004 (2004) 2180–2188.
- [18] F Chen, X Lu, X Chen, H Li, Y Hu, Synthesis, structures and ethylene polymerization activity of chromium(III) complexes with N,O,N'-tridentate ligands, *Inorganica Chim. Acta.* 387 (2012) 407–411.
- [19] T Misawa-Suzuki, R Ikeda, R Komatsu, R Toriba, R Miyamoto, H Nagao. Geometry and electronic structures of cobalt(II) and iron(III) complexes bearing bis(2-pyridylmethyl)ether or alkylbis(2-pyridylmethyl)amine, *Polyhedron* 218 (2022) 115735.
- [20] SO Ojwach, B Omondi, J Darkwa. Bis(pyridin-2-ylmeth-yl) ether]trichlorido-rhodium(III) dichloro-methane monosolvate: unusual hydrolysis of the methyl-ene bridge in (pyrazolylmeth-yl)pyridine, *Acta Crystallogr. Sect. E. Struct. Rep. Online* 67 (2011) m1097.
- [21] D Nanty, M Laurent, MA Khan, MT Ashby. Fac-Tricarbonyl[bis(2-pyridylmethyl)ether-N,O,N']molybdenum(0), *Acta Crystallogr. C* 56 (Pt 1) (2000) 35–36.
- [22] JM Li. Dichlorido{2,2'-[oxydi(methylene)]dipyridine- $\kappa^3\text{N,N,N}'$ }cadmium(II), *Acta Crystallogr. Sect. E. Struct. Rep. Online* 63 (2007) m2241.

- [23] JM Li. Dichlorido[2,2'-(oxydimethyl-ene)dipyridine]zinc(II), *Acta Crystallogr. Sect. E. Struct. Rep. Online* 64 (2008) m1468.
- [24] JJ Derringer, DC Bebout. Crystal structure and Hirshfeld surface analysis of dichlorido {2, 2'-[oxybis (methylidene)] dipyridine} mercury (II), *Acta Crystallogr. E: Crystallogr. Commun.* 78 (2022) 1233–1237.
- [25] Cambridge Structural Database, 5.43 (2021).
- [26] C Hübschle B., GM Sheldrick, B Dittrich. ShelXle: a Qt graphical user interface for SHELXL, *J. Appl. Cryst.* 44 (2011) 1281–1284.
- [27] WC Wolsey. Safety in the chemical laboratory XCXIII. Perchlorate salts, their uses and alternatives, *J. Chem. Educ.* 50 (1973) a335–a337.
- [28] KN Raymond. Tragic consequence with acetonitrile adduct, *Chem. Eng. News* 61 (1983) 4.
- [29] D Ninković B., G Janjić V., S Zarić D., Crystallographic and ab Initio Study of Pyridine Stacking Interactions. Local Nature of Hydrogen Bond Effect in Stacking Interactions, *Cryst. Growth Des.* 12 (2012) 1060–1063.
- [30] H Wu, R Yun, K Wang, X Huang, Q Sun. 1,3-Bis(1-benzyl-1H-benzimidazol-2-yl)-2-oxapropane, *Acta Crystallogr. Sect. E. Struct. Rep. Online* 65 (2009) o1014.
- [31] H Wu, F Kou, F Jia, B Liu, J Yuan, Y Bai. Synthesis, Crystal Structure and DNA-Binding Properties of a Zinc(II) Complex with 1,3-Bis(1-propylbenzimidazol-2-yl)-2-oxapropane, *J. Chem. Crystallogr.* 42 (2012) 884–890.
- [32] H Wu, F Kou, F Jia, J Yuan, B Liu. Bis[1,3-bis-(1-methyl-1H-benzimidazol-2-yl)-2-oxapropane]-cadmium dipicrate acetonitrile sesquisolvate 0.25-hydrate, *Acta Crystallogr. Sect. E. Struct. Rep. Online* 67 (2011) m647.
- [33] H Wu, F Kou, F Jia, B Liu, J Yuan. Bis[1,3-bis(1-propyl-1H-benzimidazol-2-yl)-2-oxapropane]-cadmium(II) dipicrate dimethyl-formamide monosolvate, *Acta Crystallogr. Sect. E. Struct. Rep. Online* 67 (2011) m1461.
- [34] H Wu, B Liu, F Kou, F Jia, J Kong. Bis[1,3-bis-(1-ethyl-1H-benzimidazol-2-yl)-2-oxapropane]-cadmium(II) dipicrate dimethyl-formamide disolvate, *Acta Crystallogr. Sect. E. Struct. Rep. Online* 67 (2011) m768.
- [35] P Pyykkö, M Straka. Ab initio studies of the dimers (HgH₂)₂ and (HgMe₂)₂. Metallophilic attraction and the van der Waals radii of mercury, *Phys. Chem. Chem. Phys.* 2 (2000) 2489–2493.

- [36] A Bondi. van der Waals Volumes and Radii, J. Phys. Chem. 68 (1964) 441–451.
- [37] MK Rofouei, Synthesis, characterization and crystal structures of HgII complexes with asymmetric ortho-functionalized 1,3-bis(aryl)triazene ligands, Polyhedron 44 (2012) 138–142.
- [38] MK Rofouei, Z Ghalami, J Attar Gharamaleki, V Ghoulipour, G Bruno, HA Rudbari. Synthesis, Structure, and Solution Study of a Mercury(II) Complex with the Ligand [1-(2-Methoxyphenyl)-3-(4-chlorophenyl)]triazene, Z. Anorg. Allg. Chem. 638 (2012) 798–803.
- [39] MK Rofouei, E Fereyduni, J Attar Gharamaleki, G Bruno, H Amiri Rudbari. Bis[1-(2-eth-oxy-phen-yl)-3-(4-nitro-phen-yl)triazenido]mercury(II), Acta Crystallogr. Sect. E. Struct. Rep. Online 66 (2010) m1082.
- [40] RD Pike, DC Bebout. Synthesis and Characterization of an Unusual High Coordination Number Alkylmercury Complex with Topologically Linear Ligand, J. Chem. Crystallogr. 46 (2016) 324–329.
- [41] DB Tice, RD Pike, DC Bebout. Contrasting coordination behavior of Group 12 perchlorate salts with an acyclic N₃O₂ donor ligand by X-ray crystallography and ¹H NMR, Dalton Trans. 45 (2016) 12871–12883.
- [42] H Lu, W Wang, X Tan, X Luo, M Zhang, M Zhang, S Zang. A new quinoline-based fluorescent probe for Cd(2+) and Hg(2+) with an opposite response in a 100% aqueous environment and live cell imaging, Dalton Trans. 45 (2016) 8174–8181.